Check for updates

Random alloy and intermetallic nanocatalysts in fuel cell reactions

Junming Zhang,† Linfan Shen,† Yanxia Jiang ⓘ * and Shigang Sun ⓘ *

Fuel cells that use small organic molecules or hydrogen as the anode fuel can power clean electric vehicles. From an experimental perspective, the possible fuel cells' electrocatalytic reaction mechanisms are obtained through *in situ* electrochemical spectroscopy techniques and density functional theory calculations, providing theoretical guidance for further development of novel nanocatalysts. As advanced nanocatalysts for fuel cells' electrochemical reactions, alloy nanomaterials have greatly improved electrocatalytic activity and stability and have attracted widespread attention. Enhanced electrocatalytic performance of alloy nanocatalysts could be closely related to the synergistic effects, such as electronic and strain effects. Depending on the arrangement of atoms, alloys can be classified into random alloy and intermetallic compounds (ordered structure). Intermetallic compounds generally have lower heats of formation and stronger heteroatomic bonding strength relative to the random alloy, resulting in high chemical and structural stability in either full pH solutions or electrochemical tests. Here, we summarize the latest advances and the structure–function relationship of noble metal alloy nanocatalysts, among which Pt-based catalysts are the main ones, as well as comprehensively understand why they significantly affect the electrocatalytic performance of fuel cells. Novel alloy nanocatalysts with a robust three-phase interface to achieve efficient charge and mass transfer can obtain desirable activity and stability in the electrochemical workstation tests, and is expected to acquire a higher power density on fuel cell test systems with harsh test conditions.

1. Introduction

Research on the electrocatalytic energy conversion processes has been increasing due to the reduction in energy reserves and concerns over sustainable technological developments such as fuel cells (FCs).[1–3] In the past few decades FCs have made great progress, however their commercialization has been impeded by factors such as high cost, insufficient life expectancy, and low power density. Heterogeneous electrocatalysts play a crucial role in FCs as a result of improving the rate, efficiency and selectivity of the chemical transformations involved.[4,5] The electrocatalytic performance of almost all nanocatalysts is heavily dependent on the binding strength between the reactive species and the active sites on the catalyst surface.[6] Therefore, the rational design of heterogeneous electrocatalysts by controlling their structure–function relation-

ships has received extensive attention. Among all the single metals used in FC systems, platinum is considered to be the most effective electrocatalyst; however, its high cost and sensitivity to CO poisoning hamper its practical application.[7–9] At present, to incorporate other metals into Pt atoms is an effective strategy for adjusting the surface electronic effects and spin density distribution, increasing CO tolerance, and enhancing the electrocatalytic performance.[10,11] Improved synthesis approaches for various alloy nanomaterials have been explored to realize the practical application, which has been demonstrated in some excellent reviews.[12–14] Generally, as-synthesized Pt-based or Pd-based alloys have a face-centered cubic (fcc) structure, and two atoms randomly occupy the crystal lattice, whereas intermetallic compounds possess unique properties, including well-defined atomic ratios and long-range ordered atomic arrangement of the entire nanoparticle, in which the key for controlling ordered structures is usually through appropriate high-temperature treatment.[15–19] Pt-based or Pd-based intermetallic compounds have specific crystalline phases, such as face-centered tetragonal (fct),[20,21] simple cubic (sc),[22,23] body-centered cubic (bcc),[24,25] hexagonal close packed (hcp),[26,27] and so on, which can be visually confirmed through

State Key Laboratory of Physical Chemistry of Solid Surfaces, Department of Chemistry, College of Chemistry and Chemical Engineering, Xiamen University, Xiamen 361005, People's Republic of China. E-mail: yxjiang@xmu.edu.cn, sgsun@xmu.edu.cn
†These authors contributed equally to this work.

powder X-ray diffraction (XRD) and cs-corrected transmission electron microscopy (TEM). Here, we emphasize the structure–function relationship of the latest noble metal alloy nanocatalysts and their high-efficiency applications in various fuel cell electrochemical reactions.

With the development of synthetic methods, the study of the structure–function relationship can be conducted in more detail. Electrocatalytic reactions are quite sensitive to the surface structure of nanocatalysts, thereby metal nanomaterials with different sizes, shapes, and compositions can directly regulate the electrocatalytic activity and durability.[28–30] For the particle size of catalysts, reducing the particle size results in a maximum surface-to-volume ratio, and more reactive sites appear on a given alloy. Meier *et al.* studied the relationship between particle size and electrochemical proton reduction performance by scanning tunneling microscopy combined with electrochemical tests.[31] As the particle size of Pd nanoparticles decreases from 200 to 6 nm, the catalytic activity is enhanced by more than two orders of magnitude. Thus, an appropriate particle size is important for electrocatalytic reactions, and 2–5 nm Pt-based alloy nanocatalysts have better oxygen reduction reaction (ORR) activity.[32] Smaller nanoparticles are more likely to form alloys due to the faster diffusion between heteroatoms. When the particle size of alloys is increased to a certain size, the solubility of heteroatoms decreases, accompanied by the appearance of surface segregation. Except for some surfactants and nanocarbon materials, mesoporous silica or zeolitic imidazolate frameworks also were used as a coating to control nanoparticles with a smaller size at higher annealing temperature, such as PtZn nanoparticles.[33,34]

Beyond that, metallic nanomaterials with specific crystal facets have also received extensive interest due to their enhanced electrocatalytic properties.[35] Nanocrystals with specific crystal facets can provide some active sites similar to edges, corners, kinks, and so on.[36–38] And the shape of nanocrystals strongly depends on thermodynamic and kinetic parameters. For example for fcc Pt, the surface energy order is $\gamma(111) < \gamma(100) < \gamma(110) < \gamma(hkl)$, where (hkl) represents high-index faces with at least one Miller index greater than 1.[39] From a thermodynamic point of view, crystal faces with high surface energy are unstable; the catalysts usually obtained by the simple liquid-phase synthesis method are spherical nanoparticles, thus it is difficult to synthesize catalysts with special crystal planes. However, Sun *et al.* have developed an electrochemical square wave potential method to synthesize polyhedral Pt nanocrystals enclosed by {730}, {210} or adjacent high-index crystal faces, which exhibited higher electrocatalytic activity than common nanostructures.[40–42] Excavated cubic PtIr alloys with high {710} crystal faces were also successfully synthesized in a deep eutectic solvent by the electrochemical method.[43]

In addition, controlling the relationship between alloy composition and electrocatalytic performance is more complicated, because factors such as atomic ratio, crystal phase, and the degree of ordering all affect the electrocatalytic perform-

ance. For example, $Pt_{100−x}Fe_x$ alloys with various compositions were prepared by chemical reduction, in which the $Pt_{50}Fe_{50}$ nanocatalysts exhibited the highest electrocatalytic activity and long-term stability towards formic acid electrooxidation.[44] Pt_3Zr alloy with an hcp crystal structure was obtained by annealing fcc Pt_3Zr nanoparticles at 1000 °C, the former exhibited better electrocatalytic performance toward the ethanol oxidation reaction (EOR) than the latter and commercial Pt/C.[45] The characterization results of hard X-ray photoemission spectroscopy showed that the hcp structure resulted in a stronger interaction between Pt and Zr atoms, and increased the surface energy which is beneficial for the electrocatalytic oxidation process. Moreover, Pd_3Pb intermetallic compound with a nanowire network structure was synthesized, and its catalytic performance for the ORR and EOR was enhanced compared with Pd black.[46] For the EOR, the mass activity of the intermetallic Pd_3Pb was about twice that of Pd black, and it also exhibited excellent resistance to methanol and CO as the cathode catalyst. The higher electrocatalytic performance was partially attributed to the defect-rich porous architecture and ordered structure that provided abundant active sites, accelerated mass diffusion rates, and improved the electronic effect. In brief, the design principles (*i.e.*, size, shape, composition, *etc.*) of catalyst materials are fully developed for the efficient FC reaction.

Among them, the synergistic effects are known to achieve the above advantages: strain effects and electronic effects.[47–51] In Pt-based alloys, Pt atoms can be purposefully controlled to accumulate on the surface of the alloy and then form surface strain, which can markedly affect the corresponding electrochemical activity. As the thickness of the Pt-shell increases, this strain effect decreases. According to the matching degree of lattice constant, the strain can be classified into compressive strain and tensile strain.[52] The compressive strain will weaken the interaction between the catalyst surface and adsorbates.[53] Conversely, the tensile strain can cause the orbital overlap of the outer metal to decrease, the d-band center of Pt to move upwards, and the interaction between the adsorbate and catalytic surface to enhance. For instance, polycrystalline Pt_5Gd electrodes were sputter-cleaned in an ultra-high vacuum chamber, and its ORR activity increased by 5-fold that of pure Pt due to the compressive strain effect.[54] DFT calculations indicated that the compressive strain would reduce the binding strength of OH_{ads} species and provide an optimum OH binding energy of 0.1 eV, which is 2% weaker than Pt (111). Fcc PtCu alloy shells were deposited on PdCu intermetallic seed to prepare faceted core–shell (*i.e.* intermetallic-random alloy) nanocatalysts with high compressive strain, which greatly improved the ORR performance.[55] Selecting intermetallic nanoparticles as substrates can not only provide a strain effect, but also inhibit the corrosion of Cu atoms during electrochemical tests. The PtPb/Pt core–shell nanostructure with large biaxial strain also exhibited high ORR mass activity reaching 4.3 A $mg_{Pt}^{−1}$ at 0.9 V.[56] DFT calculations showed that the tensile strain optimized the adsorption energy of O species. As suggested by the previous literature, the compres-

sive strain helps to weaken the bonding strength of the OH species, while the tensile strain will optimize the strength of the Pt–O bond. Furthermore, the electrons of alloys are transferred from lower-electronegative atoms to higher-electronegative atoms, which cause the d-band center to deviate from the Fermi level and change the electron structure of surface atoms.[57–59] For example, $PdCu_3$ intermetallic compound is electrochemically dealloyed to form a Cu-free surface with a lower d-band center and oxygen binding energy than the $PdCu_3$ and Pt (111) nanostructures, which supports the excellent electrocatalytic performance for the ORR.[60] Alloys alter the surface coordination environment and electronic structure of the active sites, thereby optimizing the interaction between the adsorbates and the catalyst surface. Both the strain and electronic effects of alloys can cause the same change of atomic orbital overlap and d-band center shift, so the two effects are difficult to distinguish and are often interrelated. Adding an oxophilic metal into Pt atoms can make the adsorption potential of OH species lower than that of Pt, and then enhance the resistance to CO poisoning and electrocatalytic activity through the strain and electronic effects.

Regardless of any electrocatalytic reactions of FCs, the goals of achieving high activity and durability are the same, which can be realized by using Pt-based alloy nanocatalysts. Although random alloys exhibit enhanced electrocatalytic performance, the rapid dissolution of non-noble components can result in performance decay. As mentioned above, converting a random alloy to the intermetallic compound is an effective method to solve this problem. For example, random and ordered $PtCu_3$ alloys with the same size, composition, and particle distribution were prepared to compare their electrocatalytic performance.[61] Due to high Cu content in the alloys, the initial spherical nanoparticles become more faceted after 500 cycles, while the potentiostatic treatment will cause the spherical nanoparticles to become porous. After the cyclic voltammetry test of the 40th cycle, the electrochemical signals of Cu disappeared and a protective Pt-shell was formed rapidly for the intermetallic structure, while Cu below the surface was sequentially exposed on the surface of the random alloy. The ICP test found that the amount of Cu leaching from the random alloy was always higher than that of the intermetallic catalyst. Sun et al. have transformed the fcc-PtFe to the fct-PtFe by coating a MgO layer on the fcc-PtFe nanoparticles, which would prevent nanoparticles from sintering during the annealing process.[62] Then they compared the stability of fcc-PtFe/C and fct-PtFe/C nanocatalysts by simple acid leaching in H_2SO_4 solution. After immersing for 1 h, the Fe content in fcc-PtFe/C decreased by 36.5% while fct-PtFe/C showed only a small Fe change (3.3% loss). Taking Abruña's work as another example, a core–shell structured PtCo nanocatalyst with an intermetallic core and a 2–3 atomic-layer-thick Pt shell (Pt_3Co/Pt) was reported.[63] The specific activity of the ORR on Pt_3Co/Pt was increased by 200% and 300% relative to random Pt_3Co alloy and Pt/C. After 5000 cycles on Pt_3Co/Pt, the ORR activity loss was minimal, and the intermetallic structure remained intact. High activity and stability can be ascribed to the strain and electronic effects, leading to optimal surface–adsorbate interactions. Another method is the purposeful dealloying from Pt-based nanocatalysts, and two types of dealloying methods, namely chemical etching and electrochemical methods, can be found in the literature. After auxiliary metals are selectively leached from the near-surface region by designed pretreatment, the Pt-rich shell structure can be obtained, such as $Pt_{25}Cu_{75}$ and $Pt_{25}Ni_{75}$.[64,65] As-prepared Pt-based nanoparticles have defective Pt layers after being dealloyed; further annealing treatment at 400 °C can smoothen Pt layers to form a Pt-skin surface.[66–68] The application of dealloying methods and the improvement in the activity and stability will be described in detail in the ORR section below. Finally, surface segregation is another effective strategy to engineer the skin structure and control the alloys' surface properties by reducing the surface free energy. Many factors can greatly alter the surface energy, including temperature, adsorbate, and even substrates.[69] Sun's group synthesized well-dispersed PtBi intermetallic compound by a combination of conventional impregnation and hydrogen annealing, in which the mass activity for HCOOH electrooxidation was 10.2 and 28.1 times those of Pd black and Pt/C catalyst, respectively.[70] In subsequent work, they regulated the surface atomic composition of intermetallic PtBi and obtained the Bi-rich surface structure.[71] Both PtBi alloys are superior formic acid oxidation reaction (FAOR) electrocatalysts, and the electrochemical in situ Fourier transform infrared spectroscopy (FTIRS) results display that the FAOR on the Bi-rich surface is through the non-CO pathway. Moreover, the Pt_3Ni/PC alloy with adjustable surface composition, namely a Pt-skin and Ni-rich structure, was prepared via a controlled thermal treatment method.[72] Pt-skin and Ni-rich Pt_3Ni/PC nanostructures enhanced the catalytic activity for the ORR and FAOR, respectively, both of which are three times as active as the Pt/C catalyst. The controlled heat treatment method can be used to design catalysts with various nanostructures, such as intermetallic compounds, Pt-skin catalysts, non-precious metal-rich catalysts, etc. These nanostructures can be used for various electrocatalytic reactions to adjust the reaction pathway and the molecular adsorption mode.

So far, with the improvement of nanotechnology and characterization methods, researchers can purposely synthesize alloy nanocatalysts with specific physical properties and excellent electrochemical performance. Engineering the surface/near-surface nanostructure is a promising strategy to improve the electrocatalytic performance of alloys, which can maximize the exposure and utilization of active sites. In each section of this article, based on the combination of in situ electrochemical spectroscopy techniques and classical theoretical calculations, we discuss molecular adsorption modes, chemical bond cleaving, reaction energy barriers, coordination environments, underlying reaction mechanisms, etc. Then, the corresponding challenges in the five electrocatalytic reactions are proposed, and how can they be addressed? The development and application of Pt-based alloy nanocatalysts in recent years are discussed in detail. In particular, the electronic effect, strain effect, and ordered structure of alloys are intro-

duced to emphasize their role in improving the electrocatalytic performance, and the progress of tuning strategies and quantification methods is also described. Furthermore, some typically used strategies to improve the alloy nanostructure are also summarized, including annealing treatment, dealloying strategies, the galvanic replacement reaction, and so on, which provide useful clues for guiding the synthesis of nanocatalysts with excellent performance and durability. Designing advanced alloy nanomaterials with unique effects and structures is expected to realize the commercialization of FCs. We clarified the future prospects of alloy nanocatalysts, which are both challenges and opportunities for energy conversion.

2. Small organic molecule electrooxidation reaction

For low-temperature FCs, besides hydrogen, various small organic molecules (SOMs) can be used as anodic fuels, such as methanol, ethanol, formic acid, and so on.[73,74] As mentioned above, the issue of low efficiency of platinum catalysts can be addressed by selecting an inexpensive or earth-rich element to form alloys, which are the most versatile and effective catalysts in the anode and cathode of FCs.[75–77] For Pt-based alloys, besides strain effects and electronic effects, changes in the distance between Pt–Pt atoms and the number of adjacent Pt atoms also can adjust the bonding strength of reaction intermediates and optimize the reaction activation energy. In this section, the goal is to understand the electrocatalytic reaction mechanisms of the methanol oxidation reaction (MOR), the ethanol oxidation reaction (EOR), and the formic acid oxidation reaction (FAOR), the latest development trend of noble metal alloy catalysts, as well as the significance of the structure–activity relationship for designing advanced electrocatalysts.

2.1 MOR

Methanol is a relatively stable, economical, and easy-to-transport liquid that can be fed directly into the cell as a fuel (DMFCs).[78,79] The primary reason for the low efficiency of DMFC anode catalysts is that the CO_{ads} intermediate firmly adheres to the active sites, requiring a higher removal potential. For Pt-based nanocatalysts, it is generally accepted, despite the controversy, that the MOR has two parallel pathways: indirect CO poisoning and direct formate pathways (Fig. 1A).[80,81] A cyanide-modified Pt (111) electrode was used as a chemically modified electrode to study the role of atomic ensembles in the electrooxidation of methanol molecules.[81] Electrochemical tests and *in situ* FTIRS indicated that two adjacent platinum atoms are the smallest atomic ensemble for the MOR to CO_2 through the non-CO pathway. They also clarified that formate might be formed *via* the reaction between methanol-derived adsorbates and bulk water. The formation of CO *via* the indirect oxidation pathway requires at least three contiguous Pt atoms, and this result can help design a non-CO poisoning catalyst. For instance, the reaction free energy on different sites for each MOR electrochemical step was calculated by DFT, where PtZn (111), stepped PtZn (211) and $Pt_{24}Zn_{24}$ cluster represented terrace, edge, and corner sites, respectively.[34] All three PtZn models underwent the direct oxidation pathway, and the MOR on corner sites had smaller barriers than that on edge and terrace sites. Unlike the PtZn system, the Pt (111) underwent the indirect oxidation pathway, in which CO* was formed after continuous cleavage of C–H and O–H bonds, followed by oxidation to form CO_2. Compared with Pt atoms, the bonding strength of Zn atoms with OH* is higher, as a result the PtZn underwent a CO-free pathway ($CH_2O^* \rightarrow CH_2O^* + OH^* \rightarrow H_2COOH^* \rightarrow COOH^* \rightarrow CO_2$).

For PtRu bimetallic catalysts, the Watanabe–Motoo bifunctional mechanism is generally accepted. However, in 2015, Tong *et al.* used Ru decorated Pt thin films (Ru/Pt) as catalysts to propose a new revised bifunctional mechanism.[82] They combined *in situ* FTIRS with control experiments, which
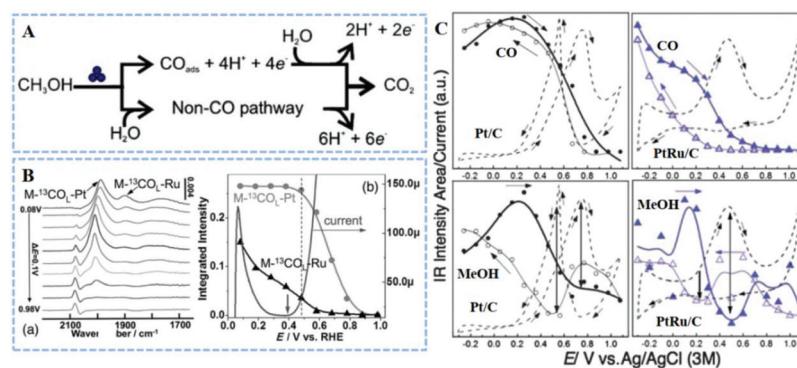

Fig. 1 (A) MOR reaction pathways. Reproduced with permission from ref. 81. Copyright 2006, American Chemical Society. (B) *In situ* ATR-SEIRAS of preadsorbed M-$^{13}CO_L$ on the Ru/Pt (M-$^{13}CO_L$ refers to the linearly bonded CO generated by methanol), and the integrated IR intensity of the M-$^{13}CO_L$-Pt and M-$^{13}CO_L$-Ru as a function of electrode potential. Reproduced with permission from ref. 82. Copyright 2015, John Wiley & Sons Ltd. (C) CO_{ads} and CH_3OH_{ads} band integrals as a function of potential in both positive and negative scans on Pt/C and PtRu/C, respectively. Reproduced with permission from ref. 84. Copyright 2012, Royal Society of Chemistry.

offered flow-cell operation and diagnostic selectivity by isotope labeling, to show that CO_L–Pt was not part of the reactions. *In situ* attenuated total-reflection-surface-enhanced IR reflection absorption spectroscopy (ATR-SEIRAS) experiments showed the onset oxidation potential of methanol molecules coinciding with formate appearance, lower than that of CO_L–Pt oxidation and higher than that of CO_L–Ru (Fig. 1B). Therefore the bifunctional mechanism (Pt-CO + Ru-OH → Pt* + Ru* + CO_2 + H^+ + e^-) has nothing to do with enhanced MOR at a lower overpotential (<0.5 V *vs.* RHE). It is worth noting that the revised reaction mechanism requires that the free Ru* and PtRu* reaction sites must be adjacent to each other and be available, and PtRu boundary sites catalyze the oxygen insertion reaction that leads to the formation of formate and undergoes the direct oxidation pathway. Furthermore, there was a dispute over the attribution of the MOR inverse-sweep peak, and recently *in situ* FTIRS techniques have provided experimental evidence. In 1992, Goodenough's group reported that the forward sweep peak (I_f) of the MOR was attributed to methanol oxidation, while the backward sweep peak (I_b) was attributed to the oxidation of residual intermediate carbon species.[83] After this work, many researchers used the peak ratio (I_f/I_b) to estimate the CO-tolerance. The origin of I_b on commercial Pt/C and PtRu/C catalysts for the MOR was investigated in-depth through cyclic voltammetry (CV) tests and *in situ* FTIRS.[84] The CO_{ads} and methanol$_{ads}$ band integrals from FTIRS as a function of potential for Pt/C and PtRu/C, along with the corresponding MOR CV, are shown in Fig. 1C. For Pt/C, the methanol molecules have been dissociated and adsorbed on the catalyst surface at a lower potential (<−0.25 V *vs.* Ag/AgCl), and generated the CO_{ads} intermediate. As the potential increases, the amount of CO_{ads} and methanol$_{ads}$ increases slightly until about 0.3 V. Then, the MOR current increases sharply between 0.3 and 0.75 V, along with the decrease of the number of CO_{ads} and methanol$_{ads}$. When the potential is higher 0.8 V, no CO_{ads} species adsorb on the surface of the catalyst. PtRu/C has a similar change as described above with the Pt/C catalyst. However, the complete oxidation on PtRu/C occurs at a lower potential than Pt/C, and the amount of CO_{ads} is much smaller than that produced in the positive, indicating that CO oxidation is easier on PtRu/C. There was a significant inverse correlation between the MOR current and the amount of CH_3OH_{ads} on the Pt/C and PtRu/C catalysts during the MOR, but the amount of CO_{ads} did not have this correlation. This indicates that both I_f and I_b are attributed to the direct oxidation of methanol, regardless of the oxidation of the remaining carbonaceous species. Moreover, electrochemical impedance spectroscopy tests showed that the reason for the CV hysteresis between the forward sweep peak and backward sweep peak is that the rate-determining step has changed, from the OH adsorption caused by water dissociation to dehydrogen of methanol.[85] They also emphasized that I_f/I_b is irrelevant to the CO tolerance, but actually related to the oxophilic degree of Pt-based nanocatalysts, such as the results in Fig. 1C.

PtRu is still the best bimetallic catalyst for the MOR, the coexisting electronic effect and the bifunctional mechanism can stimulate the chemisorption and dissociation of methanol molecules at a lower potential.[86] A highly active and durable $Pt_{72}Ru_{28}$ porous flower-like alloy, which was assembled from nanoparticles below 4.0 nm, was reported by Wang's group.[87] The specific and mass activity can reach 4.19/3.54-fold and 4.27/5.0-fold enhancement compared to those on commercial Pt black and $Pt_{50}Ru_{50}$ black, respectively. At present, its electrocatalytic performance is the highest under the same test conditions reported in the literature. Moreover, PtRu nanocrystals with a controllable shape (nanowires, nanorods, and nanocubes) were synthesized, and these {100} and {111} terminated PtRu nanocrystals were used to investigate the facet-dependent MOR electrocatalytic performance.[88] The {111}-terminated PtRu nanowires showed the highest mass activity, which was 2.28 and 4.32 times higher than those of PtRu nanocubes and commercial Pt/C, respectively, indicating that the {111} facets possess higher MOR activity relative to the {100} facets. Furthermore, the PtRu nanocatalyst (PtRu/PC-H) was annealed at a high temperature (700 °C, PtRu/PC-H) to enhance the alloying degree, thereby further improving the electrocatalytic performance of the MOR.[89] The PtRu/PC-H alloy has a higher 2θ value than that of the Pt/PC nanocatalyst in XRD, which means the occurrence of lattice contraction, and the enhancement of alloying degree after annealing. It is interesting that at annealing temperatures up to 700 °C, the as-synthesized nanocatalysts still have a small particle size (~2.82 nm) and excellent dispersibility, which may be attributed to the confined effect of porous carbon (PC) supports on nanoparticles. For the MOR, the onset oxidation potential of PtRu/PC-H shifts to a more negative value than that of the Pt/PC nanocatalyst, and the mass activity (1674.2 mA mg_{Pt}^{-1}) of PtRu/PC-H is about 4.08 times that of Pt/PC (Fig. 2A). Moreover, membrane electrode assembly (MEA) tests using PtRu/PC-H as the anode catalyst with a low Pt loading (1 mg cm^{-2}) exhibit a maximum power density of 83.7 mW cm^{-2}, which is approximately 3.1 times that of the commercial Pt/C catalyst (Fig. 2B). As seen from the *in situ* FTIRS in Fig. 2C, PtRu/PC-H alloy generates CO_2 (2345 cm^{-1}) at a lower potential of −150 mV than those on PtRu/PC-L (0 mV) and Pt/PC (50 mV) nanocatalysts, dramatically alleviating the CO_{ads} poisoning on active sites. In addition, the PtRu/PC-H nanocatalyst can easily adsorb and dissociate methanol molecules, and has a stronger bond cleaving ability of C–H and O–H.

Pt_3Ti possesses a large enthalpy of formation (ΔH_f = −298 kJ mol^{-1}), while the value of PtRu is only a few kJ mol^{-1}. Bardi and co-workers reported that the CO adsorption energy on the pure Pt surface was 5 times higher than that on the Pt_3Ti surface, implying that Pt_3Ti may have an increased CO poisoning tolerance.[90] DiSalvo *et al.* synthesized fcc-Pt_3Ti samples with a smaller size (about 3 nm) in tetrahydrofuran; then they were transformed into the intermetallic compound with a large size (~37 nm) by annealing above 400 °C.[91] CO stripping experiment shows that the CO oxidation peaks of Pt_3Ti nanoparticles are much weaker than those of pure Pt
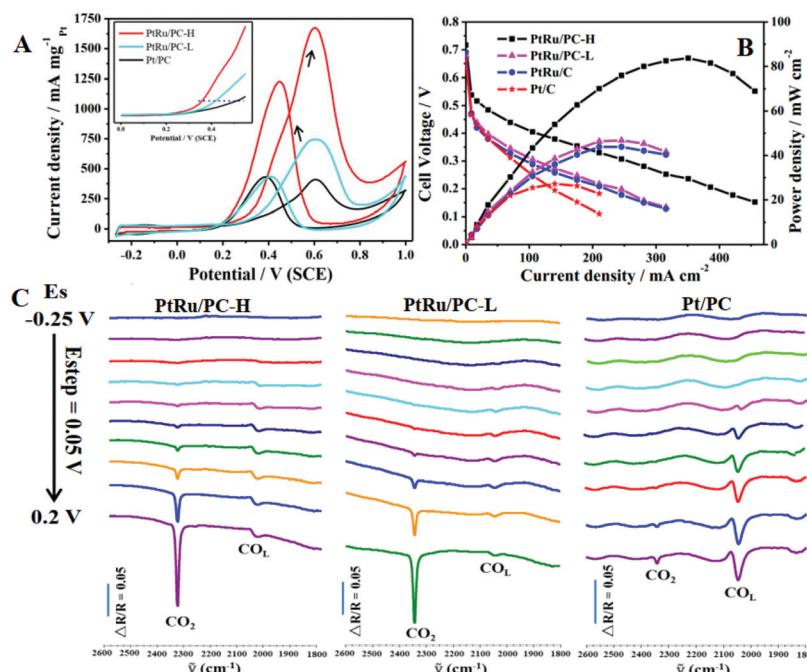
Fig. 2 (A) MOR in 0.5 M CH_3OH + 0.1 M $HClO_4$ solution for PtRu/PC–H, PtRu/PC–L, and Pt/PC nanocatalysts at a scan rate of 50 mV s^{-1}. (B) Steady-state polarization and power density curves for fuel cells employing PtRu/PC–H, PtRu/PC–L, commercial PtRu/C, and commercial Pt/C as anode catalysts. (C) *In situ* FTIRS for methanol electrooxidation on three nanocatalysts, the reference spectra were acquired at −0.27 V. Reproduced with permission from ref. 89. Copyright 2019, Elsevier BV.

and PtRu samples, suggesting that the CO affinity of Pt_3Ti catalysts is very low and the catalyst surface is difficult to poison with CO. The Pt_3Ti intermetallic compound exhibits substantially the highest electrocatalytic performance for methanol and formic acid compared to pure Pt, PtRu, and fcc-Pt_3Ti, which could be attributed to the lower CO affinity, ordered structure, and lower d-band center of Pt atoms. Moreover, they used KCl by-product as an encapsulant to control and synthesize a small-sized Pt_3Ti intermetallic compound (∼6 nm) under high-temperature annealing.[92] By increasing the annealing temperature, the ΔG of forming Pt_3Ti alloy is changed to be negative, that is, it is favorable for the formation of alloy. The mass activity of the Pt_3Ti/C intermetallic compound towards the MOR is greatly enhanced, which is about three times higher than that of Pt/C. The chronopotentiometric test shows that the intermetallic compound undergoes a small potential change for 1 h at 1 mA cm^{-2}, which may be attributed to the strong anti-toxicity and stable surface structure. Shanmugam *et al.* also fabricated Pt_8Ti intermetallic compound supported on N-doped carbon (Pt_8Ti–TiO_2/C), which was used as the anode catalyst for the DMFC single-cell test.[93] Pt_8Ti–TiO_2/C displayed 10 times higher specific activity than that of the commercial Pt/C catalyst, due to the presence of the intermetallic compound and corrosion-resistant TiO_2. More importantly, in the MEA test, the maximum power density of the Pt_8Ti–TiO_2/C anode catalyst is 48.7 mW cm^{-2} at 333 K, which is 1.6 times that of the Pt/C-based anode catalyst. The better MEA test

result is in good agreement with the result observed for the half-cell MOR.

Screening studies of intermetallic compounds for the MOR have been mentioned in reported literature, and have revealed that various ordered structures exhibit better MOR performance relative to random alloys.[94,95] Recently, Li *et al.* prepared the Pt_3Ga intermetallic nanocatalyst by co-reducing $Pt(acac)_2$ and $GaCl_3$, and then they tuned the strain of Pt by chemical etching to form 2–3 atomic-layer Pt-skin on the Pt_3Ga intermetallic compound (Pt_3Ga/Pt).[96] Fig. 3A shows the typical XRD patterns of XC-72 supported Pt_3Ga/Pt and Pt nanocrystals. Except for the carbon peak at around 25°, the other five diffraction peaks are attributed to the fcc structure in Pt nanocrystals. Pt_3Ga/Pt has six additional ordered diffraction peaks of (100), (110), (210), (211), (300) and (310), which match well with the Pt_3Ga intermetallic compound. Interestingly, the peak positions of Pt_3Ga/Pt have a positive shift compared to that of Pt nanocrystals, indicating that the Pt atoms cause the unit cell contraction phenomenon. The fast Fourier transform (FFT) pattern of a single Pt_3Ga/Pt shows the simultaneous existence of the (100) and (110) superlattice spots (Fig. 3B), which is consistent with the results obtained by XRD. The corresponding unit cell is Ga and Pt atoms located at the eight vertices and the centers of six facets of the cube, respectively. Through high-angle annular dark-field scanning TEM (HAADF-STEM), it can be seen that Ga and Pt atoms are arranged orderly in the nanoparticles, and the atoms of near-surface are all Pt atoms. Through theoretical calculation, the tensile strain of Pt-skin is
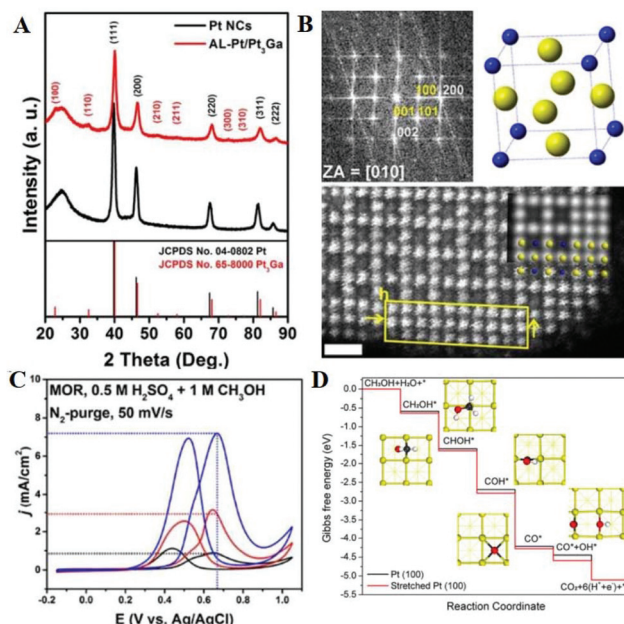
Fig. 3 (A) XRD patterns of XC-72 supported Pt_3Ga/Pt and Pt nanocrystal samples. (B) FFT pattern of the Pt_3Ga/Pt; the unit cell of the intermetallic Pt_3Ga phase, yellow and blue spheres represent Pt and Ga atoms, respectively; enlarged high-resolution HAADF-STEM images. (C) CVs of three catalysts in 1 M methanol + 0.5 M H_2SO_4 solution at a sweep rate of 50 mV s^{-1}. (D) Calculated reaction pathways of the MOR on unstrained Pt (100) and stretched Pt (100) surfaces at pH = 0.25, U = 0.88 V with respect to the RHE. The insets show the optimized structures of intermediates (Pt: yellow, C: black, O: red, H: white). Reproduced with permission from ref. 96. Copyright 2018, American Chemical Society.

3.2% along the [001] direction, while the strain along the [100]/[010] direction is negligible. The mass activity of the Pt_3Ga/Pt nanocatalyst is 3.7 and 1.9 times that of Pt nanocrystals and commercial Pt/C, respectively (Fig. 3C). After 1000 potential cycles, Pt_3Ga/Pt nanocatalyst had a negligible loss in mass activity, demonstrating its excellent stability. DFT calculations are also used to study the reaction mechanism of the MOR on the surface of tensile strained and unstrained Pt nanocrystals (Fig. 3D). On both sample surfaces, the dehydrogenation of methanol is more likely to cleave the C–H bonds than the O–H bond, but the tensile strained surface is more energetically favorable than the unstrained surface. Thus, the increased activity is attributed to the stronger binding of OH* and the lower activation energy of water. Also, the strong p–d hybridization of PtGa alloy can redistribute the electrons of two atoms, weaken the bonding strength of CO_{ads}, and suppress the diffusion of lattice atoms.[97] PtGa alloy exhibits a lower d-band center and increased vacancy formation energy relative to pure Pt, implying that the accumulation of electrons around Pt atoms results in enhanced oxidation resistance and structural stability. Therefore, the overpotential and reaction rate of the MOR on platinum have been improved.

Alloy nanomaterials allow for further reducing the Pt loading, enhancing activity and resistance of CO poisoning, as well as increasing durability. These excellent performances are related to the promoted C–H and O–H bond activation, which may be caused by the strain effect, electronic effect, crystal type, ordered structure *etc*. Intermetallic compounds can separate active sites, increase the rate of methanol oxidation, and improve catalyst poisoning because CO generation from the methanol molecule requires three adjacent Pt atoms. Compared with stable metals (Au, Pd, *etc*.), oxophilic metals (Ru, Ti, Ga, Cu, Co, *etc*.) are more likely to provide adsorbed OH* species after alloying with Pt and more effective to electrooxidize methanol molecules. There is still a big gap between the intrinsic activity of Pt-based alloy catalysts and the power density of MEA.

2.2 EOR

Ethanol is of confocal interest because it is non-toxic, has a higher energy density (8.01 kW h kg^{-1}) relative to methanol (6.09 kW h kg^{-1}), and is easy to transport and store, which may lead to a carbon-neutral economy.[13,98,99] Ethanol oxidation can occur at 84 mV under thermodynamic conditions.[100] However, due to the lack of effective catalysts to promote the complete oxidation of ethanol to CO_2 without heat loss, ethanol fuels have not been widely used except for petroleum additives in traditional combustion systems. The C–C bond cleavage in ethanol molecules requires a very high dissociating energy (~350 kJ mol^{-1}).[101] Thus, electrocatalytic oxidation of ethanol to carbon dioxide has a lower selectivity than acetic acid or acetaldehyde, and Pt nanocatalysts have a CO_2 selectivity of only 0.5–7.5%.[102] The efficiency of direct ethanol fuel cells (DEFCs) is significantly decreased because the rate of cleaving of C–C bonds is very low.[103,104] Fig. 4A shows some possible pathways for the oxidation of ethanol molecules to acetaldehyde, acetic acid and CO_2.[105] The EOR through the C1 and C2 pathways is widely accepted. For ethanol molecules, the adsorption of α-C–H on catalysts is considered as the initial step, and the dehydrogenation energy barrier of α-C–H is much lower than that of the O–H bond.[106] The reaction between acetyl and OH species is an important step to form acetic acid ($CH_3CO + OH \rightarrow CH_3COOH$), but the C–C bond cleavage is the determining step in the formation of CO_2 ($CH_2CO \rightarrow CH_2 + CO$). Therefore, the acetic acid formation process requires the assistance of OH species, that is the presence of oxygen-containing species could enhance the obstacles towards C–C bond cleavage (Fig. 4B).[105] Relative to the clean Pt surface, the presence of OH and O species will reduce the rate of C–C bond cleavage by about two orders of magnitude and six orders of magnitude, respectively. Adzic *et al.* deposited a Pt monolayer (Pt_{ML}) on different single-crystal surface substrates using the Cu underpotentially deposition method to study the strain and electronic effect on the EOR. During the synthesis, five single crystal surfaces (*i.e.* Au (111), Pd (111), Ir (111), Rh (111), and Ru (0001)) were used as substrates.[107] By changing the substrate, the strain and electronic effects of the Pt_{ML} catalysts are tailored. Fig. 4C shows the EOR curves of Pt (111) and Pt_{ML} electrocatalysts, and the activity of Pt_{ML}/Au (111) is four times that of Pt (111), which is caused by tensile
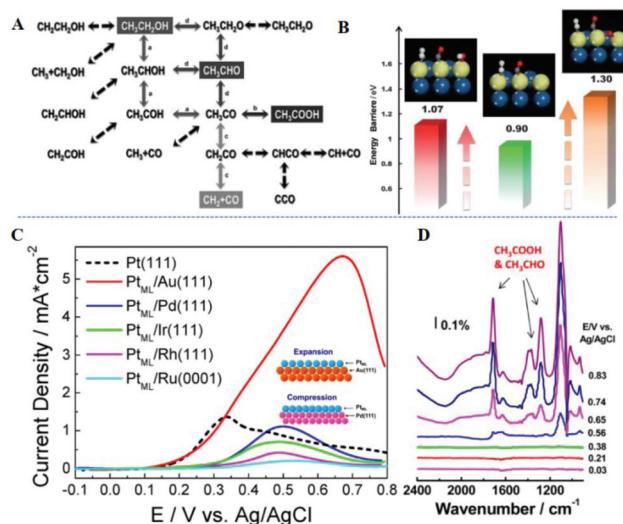
Fig. 4 (A) Reaction pathways for the formation of acetaldehyde, acetic acid, and CO_2. (B) Effect of surface oxidants (O, OH) on the key step of C−C bond cleavage. The bars are the barriers of the key step of CO formation without oxidant (green), in the presence of OH (red), and in the presence of O (brown). C in gray, O in red, and H in white. Reproduced with permission from ref. 105. Copyright 2012, John Wiley & Sons Ltd. (C) Positive voltammetric scans for Pt (111) and Pt_{ML} supported on five different substrates in 0.1 M $HClO_4$ containing 0.5 M ethanol with the scan rate of 10 mV s^{-1}. (D) In situ IRRAS spectra recorded during the EOR on the Pt_{ML}/Au (111) electrode. Reproduced with permission from ref. 107. Copyright 2012, American Chemical Society.


Fig. 5 (A) ADF-STEM image of PtSn nanoparticles, the EELS maps of Pt and Sn, and the composite PtSn map with Sn in red and Pt in cyan. (B) Comparison of EOR curves at a scan rate of 20 mV s^{-1}. Reproduced with permission from ref. 110. Copyright 2018, American Chemical Society. (C) Specific activity. (D) In situ IRRAS spectra recorded during the chronoamperometry test at 0.45 V vs. RHE for the EOR on $Pt_{38}Ir$/C. Reproduced with permission from ref. 111. Copyright 2019, American Chemical Society. (E) Variation of the ECSA of the $TaPt_3$ and Pt nanoparticles as a function of potential cycles. (F) I−V profiles and power density profiles of $TaPt_3$ and Pt nanoparticles, obtained at room temperature in 1 M ethanol solution. Reproduced with permission from ref. 113. Copyright 2015, Royal Society of Chemistry.

strain, the upshift of the d-band center, and the easy formation of OH$_{ads}$. From the in situ infrared reflection absorption spectrum (IRRAS), it can be seen the signals of acetic acid and acetaldehyde without the CO signal (Fig. 4D), indicating that Pt_{ML}/Au (111) mainly oxidizes ethanol through the C2 pathway. The following two paragraphs introduce excellent alloy nanocatalysts reported in recent years, which can oxidize ethanol molecules through C1 and C2 pathways, respectively.

Surface/near-surface engineering of alloys can effectively adjust the selectivity of ethanol electrooxidation and the optimal adsorption mode of intermediates, for example, the C−C bond cleavage activation energy of Pt (100) is 2.1 times lower than that of Pt (111).[108] Sun's group explored the EOR mechanism of PtRh nanocubes in detail. Pt_1Rh_1 alloy nanocubes show an ultrahigh mass activity, 2.48 times higher than that of commercial Pt/C at 0.4 V vs. SCE.[109] The α-C and β-C of ethanol molecules adsorbed on the neighboring Pt and Rh atoms to form CH_2CO species. This nanostructure displays efficient C–C bond cleavage and better CO_2 selectivity, due to the incorporation of Rh into the Pt lattice and the preferential (100) orientation. In situ FTIRS using isotopically-labeled ethanol further confirms that the CO_2 selectivity of Pt_1Rh_1 is 16.2 times higher than that on commercial Pt/C. Abruña et al. reported the synthesis of PtSn with a cubic core–shell morphology (more than 90% of the total).[110] Calculated by X-ray photoelectron spectroscopy (XPS), the atomic ratio of PtSn is 24 : 76 and tin oxide accounts for 79% of the total Sn, implying

that a low density and amorphous thin layer on the exterior nanocube is mainly tin oxide. In Fig. 5A, scanning transmission electron microscopy-electron energy loss spectroscopy (STEM-EELS) composition maps with simultaneous annular dark-field (ADF) images of Pt and Sn indicate that cubic PtSn contains a Pt-rich core surrounded by an Sn-rich shell that is approximately 2–3 nm thick. They further built a Pt-rich surface by electrochemical etching, sweeping 5000 cycles in acidic medium. Compared with before cycling samples, nanoparticles maintained the cubic morphology and the Pt-skin layer formed after cycling, which is a Pt-rich$_{core}$/Sn-rich$_{subsurface}$/Pt$_{skin}$ structure. This structure exhibits the highest electrocatalytic performance under potential cycling (Fig. 5B). This exceptional activity could be attributed to the electronic effect, strain effect, as well as high density Pt (100) surface sites, favoring the C−C bond cleavage. PtIr nanocubes with precisely controlled Ir-skin atomic layers were obtained through colloidal synthesis.[111] $Pt_{38}Ir$ and $Pt_{17}Ir$ nanocubes have one and two thin surface atomic layers of Ir, respectively. $Pt_{38}Ir$/C exhibits the largest current density compared to that of $Pt_{17}Ir$/C

and Pt/C catalysts, suggesting that Ir-skin with only one atomic layer is more favorable for high EOR activity. Besides, $Pt_{38}Ir/C$ also shows 4.5 times higher CO_2 selectivity at 0.85 V *vs.* RHE than that of Pt/C, which can be attributed to the combination of the crystal structure and electronic effect (Fig. 5C). The chronoamperometric test and *in situ* IRFTS are combined to study the generation of CO_2 (Fig. 5D). The $Pt_{38}Ir/C$ sample started to convert ethanol to carbon dioxide at 0.45 V *vs.* RHE after 200 s, but CO_2 could not be detected on the Pt/C catalyst even after 600 s. The DFT results also show that the PtIr (100) surface is more conducive to the C–C bond cleavage and the adsorption of $^*C_xH_yO/C_xH_y$ species. Moreover, Ta is more electropositive and oxophilic, and Pt_3Ta intermetallic compound containing a larger enthalpy of formation ($\Delta H_f = -59.5$ kJ mol^{-1}) compared with PtFe ($\Delta H_f = -13.6$ kJ mol^{-1}) can act as an effective catalyst.[112] Pt_3Ta intermetallic compound exhibited superior electrocatalytic performance compared to Pt_3Sn nanocatalysts for the EOR.[113] The Pt_3Ta sample efficiently cleaves C–C bonds and completely oxidizes ethanol to CO_2. After 10 000 cycles, Pt_3Ta retains 85% of the initial electrochemically active surface areas (ECSA) (Fig. 5E). The promoted C–C bond cleavage leads to the adsorption of CO_{ads} intermediates on the Pt_3Ta surface, and the high coverage of oxygenous species on the surface of Ta atoms facilitated the oxidation of CO_{ads} to CO_2. MEA tests demonstrate that the power density of the Pt_3Ta intermetallic compound was more than 2 times higher than that of Pt nanoparticles (Fig. 5F). Furthermore, a core–shell nanostructure with a Pt-shell on the intermetallic PtBi core was synthesized by the single-atom self-assembly method, and PtBi/Pt was supported on the graphene matrix.[114] The mass activity of PtBi/Pt for ethanol oxidation is 8.26 times higher than that of Pt/C due to the tensile strain effect. The *in situ* FTIRS and DFT results prove that the PtBi/Pt nanocatalyst can achieve the complete oxidation of ethanol molecules and obtain C1 products.

Although the C1 pathway can achieve higher electrical efficiency, the EOR is generally performed through the C2 pathway. Thus, OH species are provided to facilitate the oxidation of intermediates such as acetaldehyde. Considerable efforts have been made to optimize Pt-based nanocatalysts with the desired composition and structure. For instance, the ion irradiation technique was used to tune the defects and interfaces of intermetallic PtPb nanoplates.[115] These defects like the dislocations, subgrain boundaries, and amorphization can be controlled by changing the energy and variety of incident ions as well as the location of the beam spot. Engineered PtPb nanoplates with different defects and interfaces show the volcano-like electrocatalytic activity for the EOR as a function of ion irradiation fluence. Optimized PtPb nanoplates exhibit high EOR activity, due to the fact that this structure could undoubtedly create active sites by breaking the electron–hole symmetry. PtNi octahedral nanocrystals with an average edge length of 10 nm were synthesized.[116] The specific activity of the nanocrystal is 2.4 and 3.7 times that of conventional $Pt_2Ni/$C and Pt/C toward the EOR, respectively, indicating that the (111) facet could improve the electrocatalytic performance.

In situ FTIRS measurements show that the absorbance peak intensity of acetic acid/CO_2 on octahedra is 7.6 and 1.4 times higher than those of commercial Pt/C and conventional $Pt_2Ni/$C, respectively, implying that the octahedra show faster kinetics in the C2 pathways. Moreover, $Pt_3Co@Pt/PC$ with a 1–2 Pt-atomic-skin structure was successfully prepared by a simple controlled thermal treatment method.[117] The *d*-spacing of the edge and center is 2.27 and 2.22 Å (Fig. 6A), which is consistent with Pt and Pt_3Co (111), respectively, implying the nanocatalyst with a Pt-skin surface. Fig. 6B shows the line-profile analysis; the image confirms that the nanoparticle surface contains a large amount of Pt compared to Co and the thickness of Pt-skin is ~0.5 nm. For the EOR, the mass activity of $Pt_3Co@Pt/PC$ is 2.5 times higher than that of Pt/C (Fig. 6C), due to the bimetallic synergetic effect and unique structural advantages. To understand the impact of the strain effect on ethanol, *in situ* FTIRS contributes to recognition of the intermediates and final products, and identification of the selectivity, as shown in Fig. 6D and F. The ratio of CO_2/CH_3COOH of Pt/C first increases but decreases subsequently when the applied potentials increase. Compared with Pt/C, the value of CO_2/CH_3COOH for $Pt_3Co@Pt/PC$ is low (Fig. 6E), which suggests that the $Pt_3Co@Pt/PC$ nanocatalyst prefers breaking the α-C–H bond producing CH_3COH rather than cleaving the β-C–H bond yielding CH_2COH and obtains C2 products (such as CH_3COOH).

In brief, for Pt-based catalysts, C–C is more likely to be cleaved at low potentials, and the CO_{ads} intermediate produced through the C1 pathway needs to be eliminated by oxygen-containing species (*e.g.* OH and O species). However, the production of oxygen-containing species on the surface of the catalyst will cause the C1 pathway to be blocked and the emergence of C2 species. Thus, it is important to regulate the bonding strength and the amount of oxygen-containing species on the catalyst surface to improve the C–C bond cleavage. Furthermore, the stable intermetallic structure is of great concern, and the ordering degree can be controlled by adjusting the heat treatment procedure. Since annealing is the most versatile and effective method for converting a random alloy to an intermetallic compound, it is critical to figure out the ideal heat treatment conditions (*eg*, annealing temperature, heating rate, lasting time and gas atmosphere) for the phase conversion.[118] We have learned a lot about phase diagrams of bulk alloys from textbooks, but the practical electrocatalysts for fuel cells are often used on the nanoscale, which exhibit different behavior from the bulk form. The selectivity of ethanol oxidation products depends largely on the crystalline orientation of electrocatalysts. Therefore, it is more meaningful to study the ordered structure at the nanoscale level, and to obtain more advanced nanocatalysts that promote the C1 pathway, such as intermetallic compounds with the (100) crystal planes and strain effects.

2.3 FAOR

The theoretical energy density of formic acid oxidation is three times lower than that of methanol, but formic acid has many
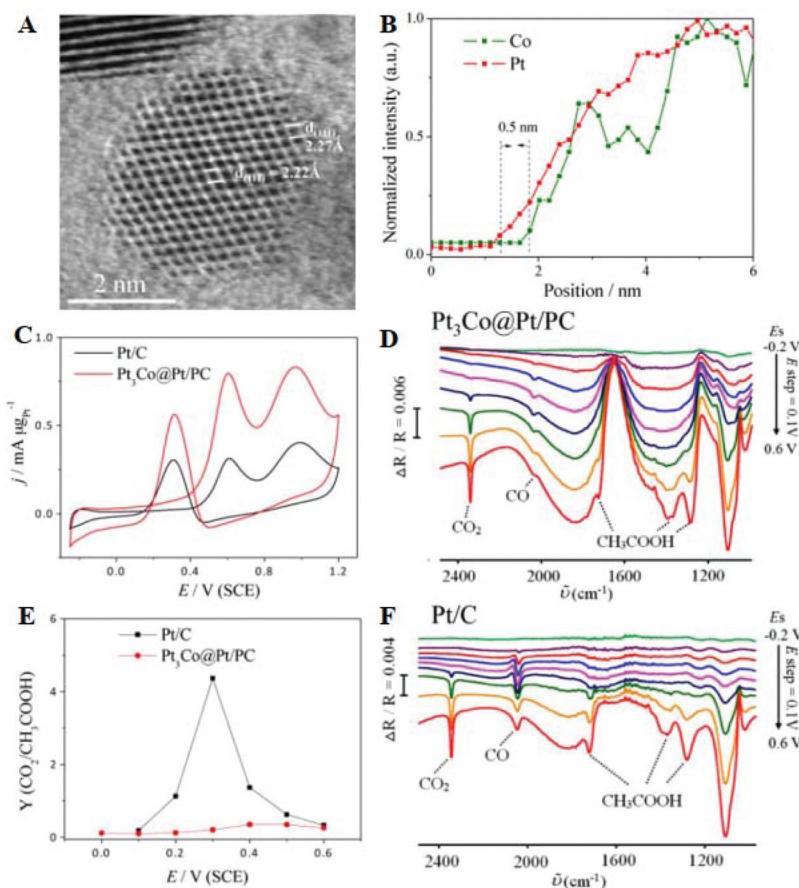
Fig. 6 (A) Atomic-resolution ADF-STEM image and (B) line-profile analysis of $Pt_3Co@Pt/PC$ nanoparticles. (C) CVs in 0.1 M CH_3CH_2OH + 0.1 M $HClO_4$ solution. (D) and (F) *In situ* FTIRS of $Pt_3Co@Pt/PC$ and Pt/C in 0.1 M CH_3CH_2OH + 0.1 M $HClO_4$. (E) Ratio of integrated intensities of CO_2 and intensities of CH_3COOH as a function of working potential. Reproduced with permission from ref. 117. Copyright 2016, American Chemical Society.

advantages as a fuel; for example, it is non-flammable, inexpensive, easily available, and stable over a wide temperature range.[119–121] Moreover, direct formic acid fuel cells (DFAFCs) have minimal anodic fuel crossover through the membrane, which is a known issue in DMFCs that can cause cathode catalyst fouling.[122] FAOR is a 2-electron transfer reaction, which can be proceeded by two different reaction mechanisms, *i.e.* the direct (dehydrogenation) pathway and the indirect (dehydration) pathway.[123–126] As shown in Fig. 7A, this involves HCOOH cleaving bonds to form a HCOOH-derivative or adsorbed CO, which is finally oxidized to carbon dioxide. Murray and co-workers combined experimental and theoretical results to prove the reason why Pt_3Pb/Pt nanocrystals could enhance the electrooxidative activity for formic acid relative to Pt.[127] For Pt (111), the first dehydrogenation step to form COOH* or HCOO* has the same activation energy barrier (0.72 eV), but HCOO* requires a much higher activation energy barrier than COOH* (1.23 *vs.* 0.71 eV) during the second dehydrogenation step, so that the stable $HCOO_{ads}$ intermediates will occupy most of the active sites and reduce the overall reaction rate. For Pt_3Pb/Pt (111), all activation energy barriers are reduced compared to the Pt (111), while the adsorption

strengths of HCOOH are enhanced, suggesting that the FAOR activity may be enhanced. Too high or low binding strength for intermediate species on the catalyst surface will hinder the kinetic process, so it is important to adjust an optimal value. Quan *et al.* also calculated the free energy of PtSn and PtBi catalysts for oxidizing formic acid through HCOO* and COOH* intermediates.[128] The DFT calculations on the PtSn model surface indicate that the dehydration pathway is easier to perform than the dehydrogenation pathway because the CO* formation energy is as low as 0.04 eV, so PtSn has a lower activity for FAOR (Fig. 7B). Compared with PtSn, the CO* formation energy on the PtBi model surface is much higher, indicating that the addition of Bi atoms plays a key role in promoting the dehydrogenation pathway (Fig. 7C). The rate-determining step for formic acid dehydrogenation on PtBi and PtSn surfaces is the first and the second dehydrogenation, respectively. Moreover, Herrero *et al.* reported that the current density of the Bi adatom-modified Pt (111) electrodes was 30–40 times higher than that of the unmodified surface towards the FAOR, and the enhancement mechanism of the Bi atoms was proved.[129] They pointed out that both Bi and Pt atoms are reactive sites. Formate chemisorbed on the Bi atoms by deprotona-
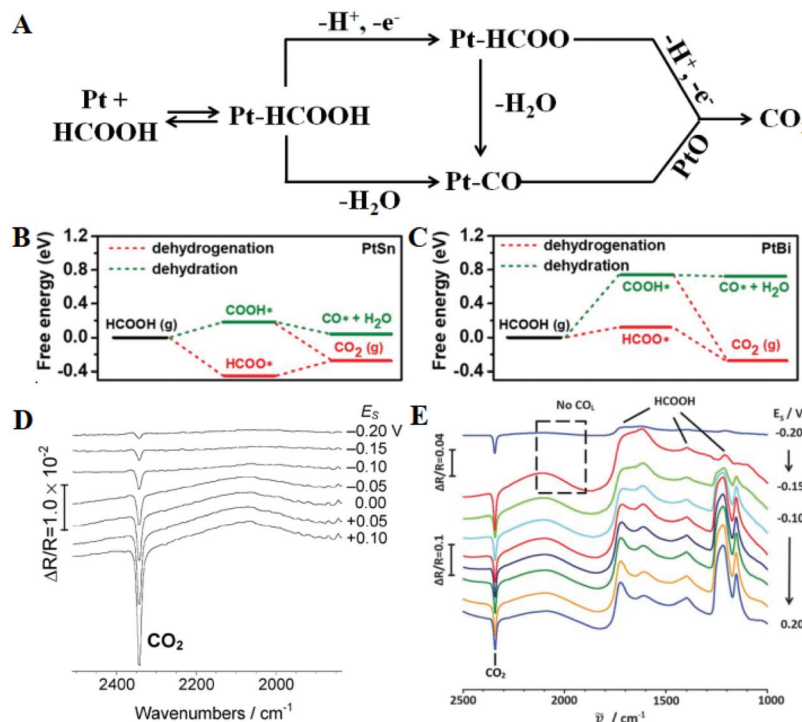
Fig. 7 (A) Dual–path mechanism for formic acid oxidation on the surface of a Pt electrode. The free energy diagrams for dehydrogenation and dehydration steps on the (100) surface of PtSn (B), and PtBi (C), respectively. Reproduced with permission from ref. 128. Copyright 2019, Wiley-Blackwell. *In situ* FTIR spectra of formic acid oxidation on Pt-BP nanocatalysts (D) and PtPb nanodendrites (E) in HCOOH + 0.1 M H_2SO_4, E_R = 0.25 V *vs.* SCE. Reproduced with permission from ref. 130. Copyright 2012, Royal Society of Chemistry. Reproduced with permission from ref. 131. Copyright 2016, Royal Society of Chemistry.

tion of the formic acid molecules, and then the C–H bond of HCOO is cleaved on the adjacent Pt site to form CO_2; Bi atoms play a decisive role in the adsorption of formic acid molecules and the further dehydrogenation of the formate intermediate. Although Pt-based catalysts generally oxidize formic acid through the CO pathway, some improved synthesis methods can change the reaction pathway. For instance, butylphenyl-functionalized Pt nanoparticles (Pt-BP) can greatly inhibit CO adsorption.[130] Electrochemical *in situ* FTIRS shows that the Pt-BP catalyst effectively blocked the CO poisoning pathway and enhanced the electrocatalytic activity towards the FAOR through the third-body effect (Fig. 7D). Furthermore, regulating the morphology of metal nanocrystals can also change the reaction pathway, such as PtPb single-crystalline nanodendrites.[131] This nanostructure shows excellent activity for the FAOR and the anti-CO-poisoning ability. In Fig. 7E, three HCOOH peaks and one CO_2 peak can be seen, indicating that the as-prepared single crystal structure oxidizes formic acid through the direct route. Thus the main methods to improve the FAOR performance include weakening the dehydrogenation barrier, enhancing the adsorption strength of reactant molecules, and eliminating CO poisoning.

Considering the FAOR of most Pt-based catalysts *via* the indirect pathway, adding oxophilic metals and engineering the surface/near-surface structure can promote CO oxidation or weaken CO adsorption by providing available OH* species at lower potentials, which help to improve the reaction rate and elelctrocatalytic performance. Li *et al.* provided a kinetically controlled method to tune the surface structure of nanocrystals, and cubic, concave cubic, and defect-rich cubic Pt_3Sn nanocrystals were synthesized.[132] Electrochemical tests confirmed the excellent FAOR performance of defect-rich intermetallic Pt_3Sn, verifying the close relationship between the catalytic activity and surface defect. Moreover, to verify the relationship between composition and crystal structure, fcc-PtAg alloys with different compositions are synthesized.[133] After $Pt_{25}Ag_{75}$ and $Pt_{51.6}Ag_{48.4}$ samples are annealed at 700 °C, their crystal structures are Ag-rich fcc alloy and intermetallic compound, respectively. $Pt_{51.6}Ag_{48.4}$ has a long-range compositional order stacking with 85% on the tetrahedral sites (hcp) and 15% on the octahedral sites (ccp). If the amount of Pt is above $Pt_{51.6}Ag_{48.4}$, the annealed bimetal separates into a Pt-rich fcc alloy and intermetallic compound. In contrast, if the Pt feeding ratio goes below 51.6/48.4 but above 25/75, an intermetallic compound and an Ag-enriched fcc-alloy are obtained. The $Pt_{51.6}Ag_{48.4}$ intermetallic compound has a 29 times higher specific activity at 0.4 V *vs.* RHE compared with Pt/C. PtAu/Pt intermetallic core/dendritic shell nanocrystals supported on the N-doped graphene support were synthesized by the wet-chemical route.[134] This catalyst displays excellent FAOR activity *via* the direct pathway, because of the large accessible surface active sites, electronic effects, as well as the introduction of a

stable N-doped graphene support. PtTe and N-PtTe intermetallic nanoparticles supported on reduced graphene oxide (rGO) were prepared by a two-step method, including the wet chemistry method and subsequent annealing under 5% H_2/Ar or NH_3, respectively.[135] The as-prepared N-PtTe/rGO shows the highest FAOR activity compared to those of commercial Pt/C and PtTe/rGO catalysts, due to the synergetic effects between the electroactive Pt and Te atoms on the surface, in which Te helps to activate OH* and allows Pt to easily oxidize the CO_{ads} species to CO_2. Importantly, N-PtTe/rGO shows more excellent durability than the other two catalysts.

Pt_xCu_{100-x} nanocubes were also successfully prepared using a colloidal approach, and the effects of the morphology and composition on the electrocatalytic properties for the FAOR were investigated. $Pt_{80}Cu_{20}$ nanocubes display the best electrocatalytic activity and remarkable long-term stability.[136] It is well known that PtBi is the most promising candidate for Pt-based binary alloys. Sun et al. have showed the catalytic activity of tetrahexahedral (THH) Pt nanocrystals, which are bound by high-index facets and possess a superior electrocatalytic activity. The performance of THH Pt nanocrystals can be further improved significantly by decorating Bi adatoms yielding the third body effect and electronic effect.[137] In comparison with bare THH Pt nanocrystals, the catalytic activity of the Bi decorated THH Pt nanocrystals has been drastically enhanced as high as 65 times at 0.4 V vs. RHE towards the FAOR. Recently, Mirkin et al.[138] developed an effective alloying–dealloying shape-regulating process to prepare a series of monometallic and bimetallic alloy THH particles, the {210} planes of which were exposed and confirmed by simulation and experiment. These THH particles were synthesized on silicon wafers or carbon supports using trace elements (such as Sb, Bi, Pb, and Te) to stabilize high-index facets. As shown in Fig. 8A, four Pt-based THH with a particle size of about 500 nm are prepared; the evaporation or dealloying process of foreign metals is critical for generating the near-perfect THH particles. Simultaneously, this solid-phase synthesis route is useful for reestablishing the important THH structure from irregular nanoparticles. Fig. 8B shows that Bi-modified THH-shaped PtBi nanoparticles have exposed planes of {210} and the proportion of Bi is 1.2%. As is well known, the rank order of specific surface energies is (111) < (100) < (110) < (210). However, the DFT calculation results confirm that the specific surface energies of these facets changed drastically after foreign metal modification, and the specific surface energy of Pt (210)-foreign-metal is the lowest. Electrochemical tests of all catalysts are carried out in Ar-saturated 0.5 M H_2SO_4 solution (Fig. 8C); these curves show the absorption and desorption signals of H. Compared with commercial Pt/C and Pt-control catalysts, Pt-based THH displays better catalytic performance toward the FAOR (Fig. 8D). In FAOR curves, the peak I at ~0.5 V corresponds to the oxidation of formic acid via the dehydrogenation pathway, and peak II at ~0.9 V corresponds to the oxidation of CO_{ads} formed via the dehydration pathway. Moreover, the specific activity of the THH PtBi particles made from a commercial Pt/C catalyst is about 20 times that of the
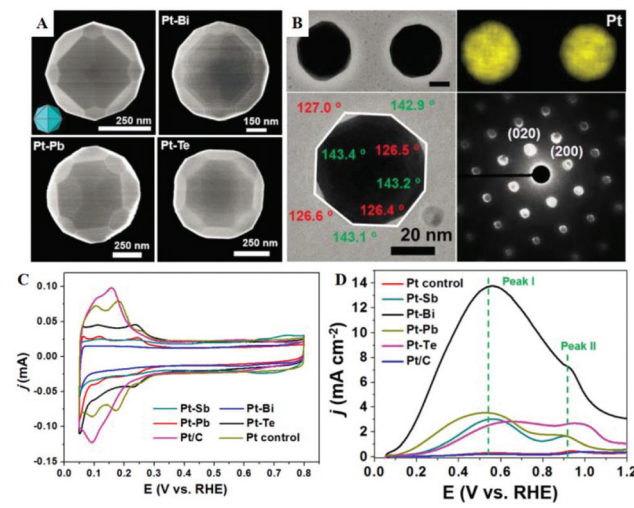
Fig. 8 (A) Representative SEM images of THH Pt, and Pt particles synthesized through Bi, Pb, and Te modification. (B) STEM images, EDS elemental maps, TEM images, and the corresponding diffraction patterns of the PtBi particles. (C) CVs of THH-shaped Pt–M (M = Sb, Bi, Pb, or Te) catalysts, Pt control sample, and commercial Pt/C catalyst in Ar-saturated 0.5 M H_2SO_4 solution. (D) Polarization curves of formic acid oxidation for different catalysts. Reproduced with permission from ref. 138. Copyright 2019, American Association for the Advancement of Science.

Pt/C catalyst at 0.5 V vs. RHE. Furthermore, Ding et al. developed an ultra-thin layer (around 100 nm) structured anode consisting of an atomic layer Bi@Pt supported on nanoporous gold, which facilitates the mass transfer and improves the utilization of Pt.[139] The maximum power density of MEA using this anode catalyst reaches ~80 mW cm^{-2}, which is twice that of the Pt/C catalyst.

Alternatively, Pd-based nanocatalysts can directly oxidize HCOOH to carbon dioxide via the dehydrogenation pathway.[140–142] Tang et al. have developed a novel carbon-supported cyanogel (C@cyanogel)-derived strategy to fabricate the Pd_3Fe/C intermetallic compound; this method could effectively suppress the movement of Pd and Fe atoms in the crystal and benefit the formation of an ordered structure.[143] The as-prepared intermetallic Pd_3Fe/C exhibited high electrocatalytic activity (696.4 mA mg^{-1}) for the FAOR relative to the fcc-Pd_3Fe/C (493.9 mA mg^{-1}) and commercial Pd/C (364.6 mA mg^{-1}) nanocatalysts, which can be ascribed to the ordering structure and electronic effect. Hollow PdAg nanostructures with exposed [100] facets can be obtained by a galvanic replacement between Ag nanocubes and Pd precursor.[144] The atomic ratio of the as-synthesized PdAg samples is controlled by changing the addition amount of the K_2PdCl_4 precursor, and the nanobox gradually becomes a hollow structure with the increase of Pd content. The FAOR activity of these samples showed an intuitive volcanic relationship with the Pd content, and PdAg alloys with a Pd content of 0.317 show the highest activity due to electronic effects and enhanced HCOO adsorption. PdCu nanosheets (thickness is about 2.8 nm) were pre-

pared by the wet chemical method, and post-treatment using ethylenediamine (EN) can remove the surfactant on the catalyst surface.[145] After ligand exchange experiments, EN exchanges oleic acid on the nanosheets. EN is an electron donor, so EN-treated samples are helpful for the adsorption of electron-deficient intermediates. The EN-treated sample has a Pd/Cu atomic ratio of 20 : 3, and the highest ECSA and mass activity, namely about 139.8 m^2 g_{Pd}^{-1} and 1655.7 mA mg_{Pd}^{-1}, respectively. The above examples demonstrate the advantages of Pd-based catalysts towards FAOR, but the stability of Pd-based catalysts is poor, and the electrocatalytic activity is not as high as Pt-based catalysts.

Adding other oxophilic metals into Pt atoms could improve the FAOR performance through the electronic effect, strain effect, and ordered structure and more importantly, optimize the binding strength between the active sites and the reaction intermediates. Moreover, alloys have a lower affinity for the CO poisoning intermediate, so formic acid is more likely to be directly oxidized to CO_2 *via* the dehydrogenation pathway.

## 3. Hydrogen–oxygen fuel cell electrocatalytic reactions

Clean and efficient alternative FC technologies have been extensively researched and developed in generation plants and automotive vehicles.[146] The anodic hydrogen oxidation reaction (HOR) of FCs is one of the best-studied reactions, and the reaction is very rapid in the presence of a Pt-based catalyst.[147] One of the greatest problems with HOR in acidic medium is the deactivation of Pt-based catalysts by small amounts of CO; CO present in the fuel as an impurity as the industrial hydrogen is produced by reforming hydrocarbons.[148] Realization of the hydrogen economy depends on efficient hydrogen production, storage, and utilization. In alkaline environments, the HOR kinetics are more sluggish by about 2 orders of magnitude than in acid medium, most likely due to the co-adsorption of cations on active sites.[55,149] At the cathode, a higher overpotential is required to meet the actual current density, accompanied by an open-circuit voltage significantly below 1.23 V. To overcome the problem of slow ORR kinetics, the cathode Pt loading needs to be increased to 8 times of the anode to achieve the desired FC performance.[56,150] A high power density (>1.0 W cm^{-2}) in MEA is the key to FC vehicle operation, but it is often limited due to low mass and charge transfer efficiency. Electrocatalysts used in practical FCs are limited by the harsh testing conditions, so it is necessary to develop efficient and more durable nanomaterials.[151–153] The goal of this section is to provide an overview of noble metal alloys used in the ORR and HOR, with a summary highlighting the future directions for this field.

3.1 ORR

In contrast to the anodic counterpart, the largest obstacle to the practical use of FCs is the sluggish reaction kinetics for the cathodic ORR.[154–157] In 2020, the target mass activity and acceptable durability for the U.S. Department of Energy are >0.44 A mg^{-1} at 900 $mV_{iR\text{-}free}$ and <40% loss in mass activity after 30 000 cycles, respectively.[158] Researchers around the globe are therefore investing much effort to develop both active and durable industrial electrocatalysts beyond the state-of-the-art Pt/C reported to date.[159–164] Enhanced activity of alloy catalysts is due to the reduced adsorption energy of the blocked OH_{ads} by the electronic effect, strain effect, and ordered structure, resulting in a greater number of active sites available for the ORR. A long-standing problem in the study of the ORR has been to determine the reaction mechanism behind the electrocatalytic enhancement. The ORR is a complex process, in which the adsorption of OOH*, O* and OH* species is a key factor in kinetics. Three predominant ORR pathways are shown in Fig. 9A.[165,166] The ORR on the Pd (111) surface is carried out through the dissociation and adsorption of O_2 molecules in the presence of a hydrated proton (Fig. 9B).[167] Protonation of O_{ads} to form OH_{ads} on the surface of Pd (111) has been suggested as the main rate-determining step. The kinetics of the ORR is strongly related to the exposed crystal plane of the nanocatalyst, and the activity of Pt (*hkl*) increases in the sequence of (100) < (110) < (111).[168] *In situ* electrochemical surface-enhanced Raman scattering (EC-SERS) was used to obtain direct evidence at the Pt (111) surfaces, reported by Tian's group.[169] The *in situ* EC-SERS spectrum on the Pt (111) electrode from 1.1 V to 0.5 V is shown in Fig. 9C. The Raman signals at around 732 and 933 cm^{-1} were ascribed to $\nu s.$ (HO_2^*) and $\nu s.$ (ClO_4^-), respectively, and HO_2^* intermediates are stably adsorbed on the Pt (111) surface. As shown in Fig. 9D, the Raman band at 732 cm^{-1} appears at a potential below 0.8 V, and increases as the potential is made less positive. Therefore, the ORR reaction mechanism is as follows: adsorbed O_2 on the Pt (111) surface forms the HO_2^* intermediate through proton and electron transfer, and then dissociates into OH* and O* intermediates, and finally the OH* species is converted to H_2O (Fig. 9E). From the above description, we can find that the reaction mechanism and the rate-determining steps are largely dependent on the active sites. In principle, the optimal electronic and geometric structures with the appropriate intermediate binding energy will lead to better catalytic performance.

Many advances have been made in the design of nanocatalysts to improve the activity, durability, and cost of Pt-based nanomaterials. One-dimensional bunched PtNi alloy nanospheres (BNSs) were synthesized, and then Ni species were selectively etched in acidic solution to form bundled nanocages (BNCs) with a Pt-skin.[170] Except that the precursor of Ni was not introduced, Pt nanowires (NWs) were obtained using a similar method. The TEM image (Fig. 10A) shows one-dimensional and highly dispersed PtNi-BNCs, whose length can reach hundreds of nanometers. Internal voids and dark walls with an average thickness of 2.2 nm are observed in the enlarged TEM image (Fig. 10B). And in the HRTEM images, the lattice fringe of 0.221 nm corresponds to the (111) plane of the PtNi alloy. In addition, Fig. 10C shows the appearance of high-index (211) and (311) facets with high-density steps and
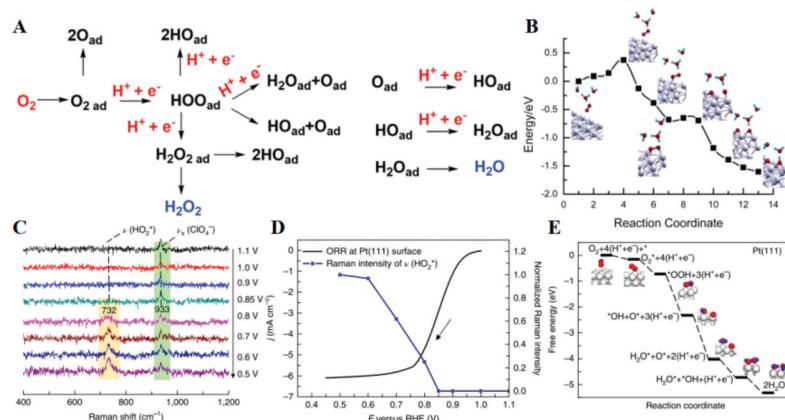
Fig. 9 (A) Schematic illustration of the possible ORR pathways. Reproduced with permission from ref. 166. Copyright 2019, Wiley-Blackwell. (B) Minimum-energy paths on the Pd (111) surface in the presence of hydrated proton. Reproduced with permission from ref. 167. Copyright 2013, American Chemical Society. (C) *In situ* EC-SERS spectra of the ORR system at a Pt (111) electrode surface in a 0.1 M HClO$_4$ solution saturated with O$_2$. (D) Normalized EC-SERS intensities of the stretching mode of O–OH around 732 cm^{-1} at different potentials. (E) The proposed ORR mechanism at Pt (111) surfaces in 0.1 M HClO$_4$ solution and relevant Gibbs free energy (eV). Reproduced with permission from ref. 169. Copyright 2018, Springer Nature.
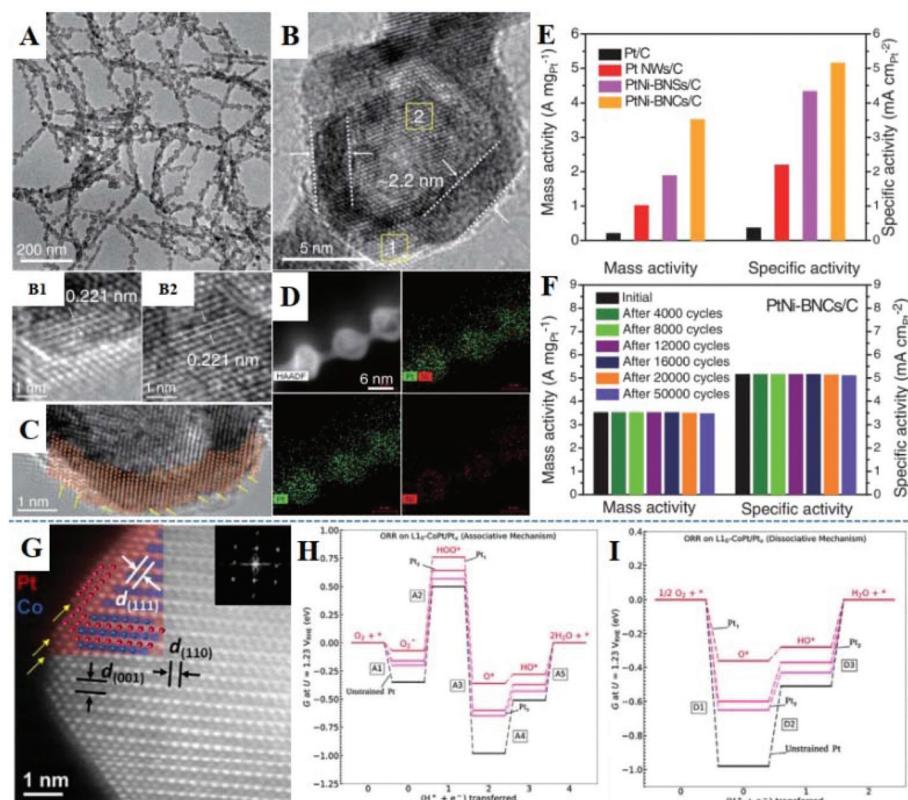
Fig. 10 (A) TEM images of PtNi-BNCs. (B) Enlarged TEM image and the corresponding HRTEM images of the areas marked by yellow squares. (C) Atomic-resolution HRTEM image. (D) HAADF-STEM images. (E) Mass and specific activities of Pt/C, Pt NWs/C, PtNi-BNSs/C, and PtNi-BNCs/C at 0.9 V *vs.* RHE. (F) Mass and specific activity evolutions of PtNi-BNCs/C. Reproduced with permission from ref. 170. Copyright 2019, American Association for the Advancement of Science. (G) Enlarged STEM image of L1$_0$–CoPt/Pt nanoparticles, Pt is colored in red and Co is colored in blue. The free energy diagram calculated *via* the DFT method on the associative pathway (H) and on the dissociative pathway (I) for the L1$_0$–CoPt/Pt$_x$ (111) surface (x = 1–3 Pt overlayers) and the unstrained Pt (111) surface. Reproduced with permission from ref. 171. Copyright 2019, Cell Press.

edges. STEM-EDS elemental mapping (Fig. 10D) further confirms the Pt-skin structure with 2–3 atomic layers of the wall in BNCs. Fig. 10E shows the ORR activity of four catalysts: PtNi-BNCs/C, PtNi-BNSs/C, Pt NWs/C, and Pt/C; the BNC nanostructure exhibits the highest mass and specific activity of 3.52 A mg_{Pt}^{-1} and 5.16 mA cm_{Pt}^{-2}, which are about 17 and 14 times higher than commercial Pt/C, respectively. The PtNi-BNCs/C catalyst also exhibits excellent durability, after 50 000 cycles, the activity decay is negligible (less than 1.5%) (Fig. 10F). This work also studied the synergistic effect of strain and the coordination number on the d-band center through in situ X-ray absorption fine structure (XAFS) technology and DFT calculations, indicating that PtNi alloy nanostructures have weaker Pt–O bonds and the optimal adsorption energies compared to Pt. In addition, compared with PtNi-BNSs/C, both the Pt–Ni coordination number and the Pt–Pt bond length for PtNi-BNCs/C catalysts are slightly reduced. Sun et al. used 8 nm PtFe intermetallic nanoparticles as a model catalyst to form core–shell FePt/Pt nanoparticles with about 2 atomic layers of Pt shell, in which Fe has better stability.[66] This FePt/Pt intermetallic compound showed excellent mass activity and better durability for the ORR in 0.1 M $HClO_4$ solution (at 60 °C) and in the MEAs at 80 °C. According to the half-cell ORR test, the mass activity is 0.7 A mg^{-1} at 0.9 V; and the mass activity shows no obvious loss after 30 000 fuel cell testing cycles between 0.6 V and 0.95 V in the MEAs, reaching the DOE 2020 target. In 2019, they reported CoPt/Pt nanoparticles with a tetragonal intermetallic core and 2–3 atomic layers of strained Pt shell as a highly active and durable ORR catalyst.[171] The structure was prepared by converting 9 nm fcc-CoPt into a CoPt intermetallic compound (ordered degree: 88%), followed by acid etching at 60 °C and annealing at 400 °C. In Fig. 10G, the STEM image shows that the structure is formed with the core containing alternative layers of Pt and Co and the shell being 2–3 atoms thick of Pt. ICP analysis shows that the Co composition in CoPt/Pt dissolved 10.2% in the 24-hour etching, while fcc-CoPt lost 69.4% during the 7 hours of etching time, which further demonstrates that the CoPt/Pt nanoparticles could effectively protect Co from acid corrosion. The specific and mass activity of CoPt/Pt is ~38 and ~19 times, respectively, that of commercial Pt/C. In the MEA test, the mass activity of CoPt/Pt reaches 0.56 A mg_{Pt}^{-1} with 19% loss at 80 °C after 30 000 cycles, exceeding the target of DOE 2020. For associative mechanisms, the formation of HOO* (A2) is uphill in free energy along with the protonation steps of O* (A4) and HO* (A5), as shown in Fig. 10H. For the dissociative mechanism, the two protonation steps of O* (D2) and HO* (D3) are uphill in free energy diagrams (Fig. 10I). With the decrease of CoPt/Pt overlayer thickness, the enhancement of the electronic effect further reduces the overpotential in the dissociation mechanism. For PtFe and PtCo systems, A2 and D3 are the potential limiting steps for the association mechanism and dissociation mechanism, respectively. DFT calculations indicate that the electronic effect and biaxial strain weaken the binding of all oxygenated intermediates on the Pt surface, resulting in an enhanced ORR performance.

Wu et al. developed a novel method that used ZIF-derived carbon as a Co source and C support to prepare the Pt_3Co intermetallic nanocatalyst via the thermal treatment of Pt nanoparticles supported on ZIF-derived carbon.[172] Co atoms in ZIF-derived carbon can diffuse into Pt nanoparticles through high-temperature annealing to form the Pt_3Co intermetallic compound, and the Co content in ZIF and annealing temperature are critical to the formation of intermetallic nanostructures. Moreover, Huang et al. prepared hexagonal PtBi intermetallic nanoplates using the colloidal chemistry method, which exhibited high tolerance over chemical fuels (such as CH_3OH, HCOOH, and CO).[173] In general, the ORR activity can be improved by adjusting the adsorption energy of the atomic O, and the upshift or downshift of the Pt d-band center has a great influence on this adsorption energy.

In order to reduce the cost of nanocatalysts, Pd-based alloys are used instead of Pt-based catalysts, and great efforts have been made to enhance the catalytic activity of Pd-based alloys to reach the level of Pt-based catalysts.[174,175] Pd_3Pb intermetallic compound was synthesized using a modified impregnation–reduction and heat treatment approach, and the insoluble KCl by-products could prevent the agglomeration of nanoparticles during the annealing process.[176] The experimental results show that increasing the annealing temperature and time is beneficial to form the intermetallic structure. Samples annealed at 600 °C for 24 hours are fully ordered because the ratios of the (110) to (111) peak are very close to the reference bulk X-ray pattern. The mass activity of the Pd_3Pb/C intermetallic compound is 168.9 mA mg_{Pd}^{-1} at 0.9 V, which is ~2–4 times higher relative to random Pd_3Pb/C, Pd/C, and Pt/C samples. Fcc-FePd and fct-FePd alloys were obtained by reduction annealing of core–shell Pd-Fe_3O_4 nanoparticles, and then intermetallic PdFe was subjected to Fe etching to form an fct-FePd/Pd structure.[177] When using acetic acid to etch nanoparticles at a controlled temperature (from 25 to 70 °C), the thicknesses of the Pd shell can be controlled to 0.27, 0.65 or 0.81 nm, thereby tuning the compressive strain and the binding energy of oxygen. Among the three different types of core–shell FePd/Pd samples studied, the fct-FePd/Pd-0.65 exhibits the best activity and stability for the ORR, which originates from the desired Pd lattice compression in the 0.65 nm Pd shell induced by the fct-FePd core. Atomic ordering nanoparticles exhibit significantly enhanced catalytic performance for the ORR due to the electronic effect and ordered structure. Moreover, the addition of gold atoms can cause PdCo nanoparticles to be an ordered structure during the annealing process at 800 °C, and the PdCo has a rhombohedral structure decorated with Au clusters.[178] PdMo alloy with ultrathin nanosheets (0.88 nm) was synthesized by a wet chemical method.[179] The nanostructure can achieve a larger ECSA and higher atomic utilization, resulting in the mass activity towards the ORR 327 times higher than that of commercial Pd/C. DFT calculations show that alloying, strain, and size effects all help to increase the ORR activity of PdMo nanoplatelets, as they can adjust the electronic structure to optimize oxygen binding. Research on Pd-based catalysts has also

made some progress, but their electrocatalytic activity and stability still cannot reach the level of Pt-based catalysts.

Post-treatment of Pt-based or Pd-based nanoparticles to form a Pt-rich structure will result in weaker binding of adsorbates, especially OH_{ads}, enhancing the catalytic activity and durability, as proven by the above systems. Peter Strasser *et al.* reviewed the progress in their preparation, structural characterization, and electrocatalytic performance of the dealloyed Pt-based core–shell structure.[180,181] Illustration of basic synthesis approaches is shown in Fig. 11A. The approaches of electrochemical dealloying, acid leaching, thermal annealing, and surface segregation have been mentioned above. In particular, alloy nanostructures with a Pt shell or Au-doped structure can be achieved by means of galvanic displacement. This brings the benefits of controlling the shell thickness and surface strain, thereby increasing the atomic efficiency. Abruña and Wang *et al.* have done a lot of work in the field, with K_2PtCl_4 or $KAuCl_4$ as the precursor of the galvanic replacement reaction. For example, PdCo@Pd/C core–shell nanoparticles were successfully synthesized using an adsorbate-induced surface segregation method.[182] The electrocatalytic activity of the PdCo@Pd/C catalyst towards the ORR is lower than that of Pt/C. However, the activity and stability were enhanced, after a small amount of Pt was deposited on the surface of PdCo@Pd/C nanoparticles to form a Pt-decorated PdCo@Pd/C nanocatalyst. The simple method significantly reduces the loading of Pt. Moreover, the ORR performance of PdFe nanoparticles is reasonably improved by the structural transition from the fcc-PdFe/C to fct-PdFe/C.[183] To further enhance the activity of fct-PdFe/C, a Pt layer was decorated on the nanoparticle surface forming an fct-PdFe@Pt/C structure (Fig. 11B), because the equilibrium electrode potential of the $PtCl_4^{2-}/Pt$ couple is more positive than those of the Fe^{2+}/Fe and $PdCl_4^{2-}/Pd$ couples. The mass and specific activity of fct-PdFe@Pt/C is 23.5 and 140 times higher compared to Pt/C, respectively, which can be ascribed to the strain effect and weakened oxygen affinity. Then, a series of PdFe@Pd/C nanoparticles with a tunable core composition were synthesized and decorated with ultralow amounts of Pt.[184] The bimetallic nanoparticles with optimal atomic ratio achieved 14 times higher mass activity than that of Pt/C. Compressive strain and electronic effects appear to be competitive for ORR activity and suggest a volcanic curve between activity and composition. This work thoroughly investigates the minimal Pt/Pd required for the monolayer coverage of Pt, and presented a formula to calculate the Pt layer thickness based on Pt content and nanoparticle size (Fig. 11C). Based on this calculation formula, the Pt/Pd atomic ratio of 10 nm PdFe@Pt particles must be larger than $1:2.7$ to obtain a Pt monolayer with 100% coverage, which is also true for AuCu@Pt[185] and $Pd_6CoCu@Pt/C$.[186] The PdZn/C intermetallic nanocatalyst with several atomic-layer Pd shells was transformed by random PdZn/C annealing at 500 °C, and the ORR activity was increased by three times relative to Pd/C.[187] Also, Au was incorporated into the PdZn/C intermetallic compound (Au–PdZn/C) by a galvanic replacement (Au : Pd = 1 : 40), since $AuCl_4^{3-}/Au$ has a more positive redox potential than those of the $PdCl_4^{2-}/Pd$ and Zn^{2+}/Zn couple. Au–PdZn/C exhibits a homogeneous elemental distribution of Au, Pd and Zn based on the corresponding EDX elemental line profiles (Fig. 11D), suggesting that Au is uniformly distributed through the entire particle. Unlike the Pt galvanic replacement method, Au not only galvanically replaced Pd and Zn on the surface but also entered the PdZn lattice to form a ternary alloy. After 30 000 potential cycles, the mass activity of Au–PdZn/C decreased by less than 10%, due to the ordered structure and stabilization effect of Au atoms.

In short, the platinum atom is still the most active site for the ORR, so the design and research on metal catalysts have attempted to mimic the geometric, electronic, and ordering structures of Pt. The above structures can be used to change the adsorption energy of reaction intermediates, thereby enhancing the electrocatalytic performance for the ORR, and the Pt-skin structure is an excellent configuration. Although the MEA test results of some Pt-based cathode catalysts have reached the DOE 2020 target, further efforts are needed in terms of the cost, activity and durability of nanocatalysts.

3.2   HOR

The HOR is the counter-reaction of the ORR in a hydrogen-oxygen fuel cell, which can directly convert chemical energy to electricity, and has gained more and more attention. For PEMFCs, only very small amounts of Pt are required due to its
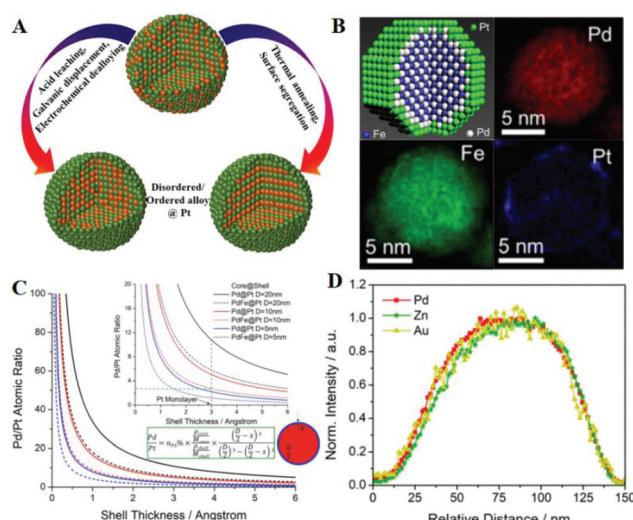
Fig. 11 (A) Illustration of the basic synthesis approaches for the preparation of Pt-skin core−shell nanoparticles (green balls: Pt, yellow balls: a less noble metal). (B) Schematic illustration of intermetallic PdFe@Pt/C, and the elemental maps of Pd, Fe, and Pt. Reproduced with permission from ref. 183. Copyright 2018, Elsevier BV. (C) Theoretical calculations of the Pd/Pt atomic ratio as a function of the particle size and the shell thickness (*x*); solid lines are Pd@Pt core−shell particles, while dashed lines are PdFe@Pt. Reproduced with permission from ref. 184. Copyright 2018, American Chemical Society. (D) STEM image and the corresponding EDX elemental maps of Pd, Zn, and Au. Reproduced with permission from ref. 187. Copyright 2019, American Chemical Society.

extremely high activity for the HOR. However, the rate of the HOR is so high in acid that the conventional rotating disk electrode (RDE) measurements cannot provide sufficiently high hydrogen mass-transport rates, due to the Nernstian diffusion overpotential.[188] Until then, 100-fold lower exchange current density values for Pt in acid were reported erroneously, generally based on RDE measurements, a microelectrode would be required to quantify kinetic rates of the HOR in acid unambiguously.[189] Indeed, in the face to the development and application of fuel cells, anode catalysts with a high CO tolerance are essential to reduce the cost of and simplify the stationary fuel cell system. In practice, Pt-based catalysts are extensively used in many electrocatalytic processes, such as we mentioned before, but they presented a weak selectivity. Currently, in industry, most of H_2 was produced from hydrocarbon reforming from fossil fuels cost-efficiently, while small amounts of CO were introduced in reformed H_2. Impurities can strongly adsorb on the Pt surface, thereby affecting the PEMFC performance and durability. Even low concentrations (~10 ppm) of CO drastically reduce the performance of PEMFCs.[190] Antipoisoning technology is critical for applications that use reformate hydrogen as a fuel. Hence, it's urgent to design Pt-based catalysts that can tolerate these poisonous species. Typically, two different ways were proposed to enhance the CO tolerance of nanocatalysts: (1) combining Pt with oxophilic metals or metallic oxides to promote CO oxidation, since the second metal can reduce the CO adsorption or OH_{ads} can accelerate the electrooxidation of CO. The classical CO electro-oxidation reaction model is the Langmuir–Hinselwood (L–H) mechanism, which can be summarized as follows:[191]

$$CO_{ads} + OH_{ads} \rightarrow COOH_{ads} \qquad (a)$$

$$COOH_{ads} + OH_{ads} \rightarrow CO_2 + H_2O \qquad (b)$$

Another CO oxidation in this onset region is relying on an Eley–Rideal mechanism where the adsorbed CO reacts with bulk water (or OH^-) and not as evidence that OH^- has adsorbed onto the catalyst surface;[192] (2) the diameters of CO molecules ~2–5 Å, allowing them to adsorb on isolated metal atoms created by molecular architectures.

The improvement of PtRu nanoparticles is one of the most promising roads to obtaining highly tolerant anode catalysts. Takeguchi et al. optimized the preparation of PtRu catalysts using a rapid quenching method and realized thoroughly mixed PtRu nanoparticles (Fig. 12A).[193] An MEA using this sample as an anode catalyst exhibits higher performance than that with conventional PtRu catalysts at a high concentration of CO. The addition of Ru contributes to CO removal, resulting in the enhancement of the efficiency of residential fuel cell systems. Zhang et al. synthesized the surface composition of Pt_3Co/C catalysts with Co-increased, the intermetallic compound, and Pt-increased by the surface segregation approach.[191] Due to the differences in the surface atomic distribution and alloying extent, the nanocatalysts show different CO poisoning tolerance in the order of Co-increased > intermetallic compound > Pt-increased. They found that the electronic
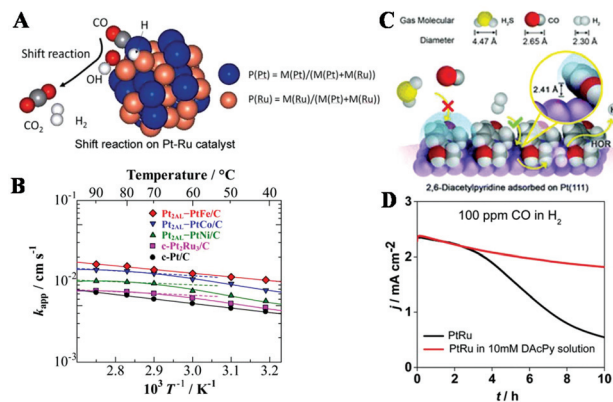
Fig. 12 (A) Schematic illustration of CO tolerance on the PtRu alloy. Reproduced with permission from ref. 193. Copyright 2012, American Chemical Society. (B) Arrhenius plots for the apparent rate constant k_{app} for the HOR (CO-free) at the Nafion-coated supported catalysts. Reproduced with permission from ref. 196. Copyright 2017, American Chemical Society. (C) The proposed model for the reduced form DAcPy adsorbed on Pt (111) from the side view. (D) CO tolerance test of commercial PtRu in 0.5 M H_2SO_4 solution with (red line) and without (green line) 10 mM DAcPy. Reproduced with permission from ref. 198. Copyright 2018, Royal Society of Chemistry.

effect plays a major role in weakening CO adsorption on Pt_3Co/C nanocatalysts and thus promoting CO oxidation to form the $COOH_{ads}$ intermediate consistent with the Langmuir–Hinselwood mechanism, and the oxophilic effect promotes the oxidation of the $COOH_{ads}$ intermediate.

However, the decrease in anode performance by the dissolution of a 3d transition metal from anode catalysts has been shown to contribute to degradation in long-term operation. There is a desire for improved durability of the anode catalyst against a high concentration of CO and/or a transient increase in the CO concentration. In particular, an anode catalyst that could tolerate a high concentration of CO could eliminate the need for a selective CO cleaner, and hence help to reduce the cost of and simplify the stationary PEMFC system. Hsieh et al. have designed well-defined Ru@Pt nanoparticles with complete, uniform Pt shells providing an opportunity to achieve the CO tolerance and corrosion resistance needed for commercializing reformate-fed PEMFCs, which was further confirmed by MEA. Their results suggest that CO tolerance can be improved by reducing the CO adsorption energy by tuning the d-band of the Pt shell.[194] Similarly, PtCo alloy with a Pt-skin structure shows highly CO-tolerant HOR activity and stability, and this enhancement is ascribed to the weak H_{ads} and CO_{ads} adsorption introduced by Co.[195] They further examined the effect of the non-precious-metal species M (M = Fe, Co, Ni) in Pt_{2AL}–Pt–M/C on the CO tolerance at 70 and 90 °C. The HOR activities increased in the order Pt < Pt_{2AL}–PtNi < Pt_{2AL}–PtCo < Pt_{2AL}–PtFe, which were ascribed to the decreasing H adsorption strength on the (111) terraces (Fig. 12B).[196] Igarashi et al. found that the surfaces of all non-precious metal alloys are composed of a thin Pt layer with an electronic structure different from that of pure Pt, indicating an

increased 5d vacancy of Pt in the layers of the CO-tolerant alloys. *In situ* FTIR spectra further demonstrate the weak bond strength between the Pt skin layer and CO, suggesting that the oxidation sites are not blocked by CO due to its enhanced H_2 mobility.[197]

Recently, a CO-tolerant anode catalyst using an organic complex as a co-catalyst is also attractive. DAcPy-modified Pt exhibits higher CO tolerance than most frequently used PtRu alloy catalysts. This molecular architecture acts as a canopy, under which Pt atoms can be accessible for small-sized H_2, but not for relatively large CO and H_2S (Fig. 12C and D).[198] This novel concept for a CO-tolerant anode catalyst using an organic complex as a co-catalyst is an attractive way for the improvement of CO tolerance. Poor tolerance to CO impurity is a drawback of PEMFCs which makes the fuel cell system complicated and expensive. The tolerance to CO impurity has attracted attention not only for the stationary applications but also for use in transportation from the viewpoint of hydrogen purity. The development of innovative and practical technology would be greatly appreciated.

Additionally, the HOR in alkaline media is more attractive and promising with the development of an alkaline membrane (OH⁻-exchange membranes) for the replacement of the noble-metal intensive PEM technology. In an alkaline electrolyte, non-noble metal catalysts are very active and stable for the ORR and the OER.[188,189] However, for yet unclear reasons, the kinetics of the HOR in the base is 1–2 orders lower in acidic pH, and large amounts of Pt are needed to catalyze the HOR in alkaline medium.[199] Correspondingly, it is under extensive debate on how the transition metals promote the alkaline HOR kinetics of Pt.[200–203] Understanding such a scientific foundation and underlying principles of alkaline electrochemistry is a critical challenge to make alkaline membrane fuel cells (AMFCs) more practical. There are currently two different views of the catalytic roles of the second metal in promoting the HOR of Pt surfaces. Despite the extensive debates within the thoughts, it is generally believed that the HOR proceeds *via* the Tafel–Volmer or Heyrovsky–Volmer mechanism in base with the Volmer step as the rate-determining step:[17,204,205]

$$\text{Tafel step}: H_2 + 2* \leftrightarrow 2H_{ads}$$

$$\text{Heyrovsky step}: H_2 + OH^- + * \leftrightarrow H_{ads} + H_2O + e^-$$

$$\text{Volmer step}: H_{ads} + OH^- \leftrightarrow * + H_2O + e^-$$
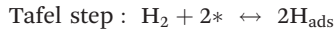
The classical model regards the hydrogen binging energy (HBE) as the only descriptor of the HOR, as represented by the Sabatier principle, that too strong or too weak of Pt–H_{ads} interaction is the disadvantage of HOR activity.[206] This view is accessible in an acid electrolyte because of the very fast reaction kinetics, however, it has been doubtful in alkaline media because of the 1–2 orders lower kinetics. The first point supports the classical model. Normally, the adsorption/desorption peak potential (E_{peak}) can reflect the Pt–H_{ads} interaction ($-FE_{peak} = \Delta H$) (Fig. 13A). Sheng *et al.* found that the HBE shows a monotonic decrease with the hydrogen oxidation activity, demonstrating that H_{ads} is the only reaction descriptor for the HOR on monometallic platinum.[207] Abruna *et al.* found that HOR activity on Pt/C and Ir/C is better than that on Ru/C and Pd/C. This is in accordance with the fact that the H adsorption/desorption process on Pt/C and Ir/C is more reversible than that on Ru/C and Pd/C (Fig. 13B).[208] As shown in Fig. 13C, the peak power density is improved to 1.0 W cm⁻² for PtRu/C as the HOR catalyst for the AMFCs, in comparison to 0.6 W cm⁻² when using Pt/C as the anode catalyst. Wang *et al.* ascribed such a remarkable improvement to electronic effects, because OH_{ads} can generate on specific sites of the PtRu/C surface at more positive potentials than on the Pt/C surface. Rather, alloying with Ru weakens the Pt–H_{ads} interaction resulting from the electronic effect demonstrated by the CVs in combination with DFT calculation, which thus supports the HBE theory.[209] Lu *et al.* studied the alkaline HOR mechanism by using pristine Pt/C, PtNi/C and PtNi/C after acid treatment (acid-PtNi/C) as the model catalysts.[210] XPS and CVs demonstrate that PtNi/C and acid-PtNi/C have similar HBE values, but weaker than Pt/C. And the OH adsorption on PtNi/C is much stronger than that on acid-PtNi/C and Pt/C. The alkaline HOR activity follows the order of acid-PtNi/C ≈ PtNi/C > Pt/C. Hence, the main reason for the enhanced HOR activities of PtNi alloys may be that the electronic effect weakens the Pt-H_{ad} interaction. Ru@Pt catalysts prepared from submonolayer to multilayer Pt coverage were used as a model system to distinguish between the bifunctional mechanism and HBE theory. It shows that the HOR activity of fully Pt-covered Ru is more active than those of partially covered Ru@Pt nanoparticles in 0.1 M NaOH. Therefore, as far as basic HOR is concerned, the role of Ru as an auxiliary metal to modify the electronic structure of Pt atoms is more important than its influence on the cleave the water. Moreover, the most active Ru@Pt core–shell nanoparticles show 4–5 times enhancement of HOR activity as compared to Pt/C, further confirming the role of lowering the H_{ads} energy barrier in the improvement of HOR activity in base.[205]

It is still uncertain the real influence of the second metal on the alkaline HOR activity of Pt surfaces. Another view is proposed by Markovic's group that they ascribed the improvement of alkaline HOR activity to the oxophilic effect. In their study, among different catalysts, both oxophilic metal (Ir) and Pt alloy ($Pt_{0.1}Ru_{0.9}$) that have an optimal balance between the active sites that contributed to the H_2 adsorption/dissociation and to the adsorption of OH_{ad} show the maximum HOR activity, in which the oxophilic sites can facilitate the adsorption of OH_{ads} species, and then react with the hydrogen intermediates (H_{ads}) (Fig. 13D).[211] Similarly, tracing Ru on commercial Pt/C can dramatically promote the HOR activity in the alkaline electrolyte. *In situ* EXAFS demonstrates the presence of OH_{ads} on the surface Ru sites in the HOR potential region and accordingly verifies the bifunctional mechanism for the HOR in alkaline medium (Fig. 13E).[212] Ruthenium-based Ru_xM_y/C (M = Pt or Pd) alloy catalysts also were synthesized to investigate the HOR in alkaline electrolytes. The exchange
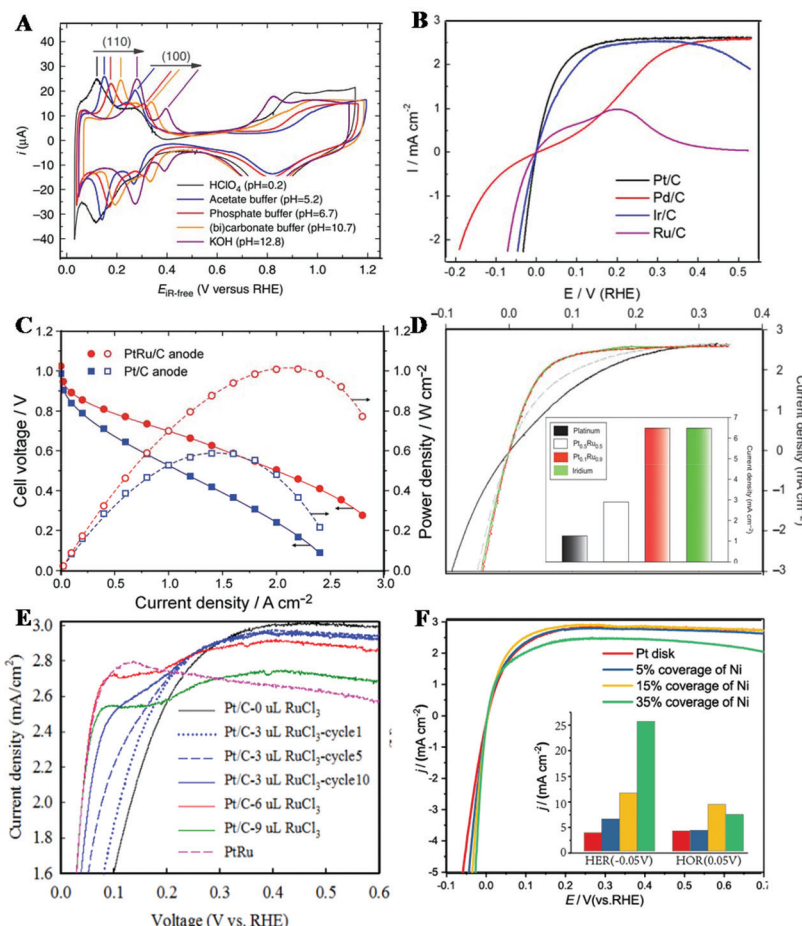
Fig. 13 (A) Steady-state CVs of Pt collected in different pH solutions. Reproduced with permission from ref. 207. Copyright 2015, Nature Publishing Group. (B) HOR polarization curves for Pt/C, Pd/C, Ir/C, and Ru/C. Reproduced with permission from ref. 208. Copyright 2017, American Chemical Society. (C) Cell performance of the AMFCs using the Pt/C or PtRu/C as the anode catalyst. Reproduced with permission from ref. 209. Copyright 2015, Royal Society of Chemistry. (D) HOR/HER polarization curves for Pt-poly (black curves) and PtRu alloys with 50% Ru (dashed grey) and 90% Ru (dashed red). The inset shows the comparison between activities at 50 mV on monometallic and bimetallic surfaces for the HOR. Reproduced with permission from ref. 211. Copyright 2013, Nature Publishing Group. (E) HOR polarization curves of Pt/C with 0, 3, 6, and 9 μL doped 5 mM $RuCl_3$ and Pt_1Ru_1/C. Reproduced with permission from ref. 212. Copyright 2017, John Wiley & Sons Ltd. (F) HER/HOR polarization curves of the Pt disk with 0%, 5%, 15%, and 35% coverage of Ni. Reproduced with permission from ref. 213. Copyright 2019, Elsevier BV.

current density on a Pt-rich $Ru_{0.20}Pt_{0.80}$/C catalyst (1.42 mA cm^{-2}) is nearly 3 times that of Pt (0.490 mA cm^{-2}). Furthermore, the Tafel slope of the Ru_xPt_y alloy in 0.1 M KOH is ~30 mV dec^{-1}, in contrast to ~125 mV dec^{-1} of Pt/C, demonstrating that H_2 dissociative adsorption is the rate-limiting step. However, Ru_xPd_y/C alloys do not change kinetics obviously. These results were attributed to the interplay of ligand and bifunctional effects. Recently, by using a bulk Pt surface decorated with different coverage $Ni(OH)_2$ and Pt–Ni model catalysts as model catalysts, Sun's group found that the rate of the HER is controlled by both the H_{ads} and OH_{ads} while the rate of the HOR is mainly determined by near-optimal H_{ads} (Fig. 13F).[213] Particularly, the electronic structure of the Ni $(OH)_2$/Pt disk will be changed with the coverage of $Ni(OH)_2$ increasing.

Overall, bimetallic systems offer a unique opportunity for designing a new generation of nanomaterials for the HOR in alkaline environments. These nanomaterials can be designed to be as active as the best catalysts in acidic media; an understanding of the fundamental mechanism will benefit the discovery of active as well as cost-effective anode catalysts for AMFCs.

4. Conclusion and outlook

In this review, we have presented the recent advancements in understanding the reaction mechanisms and designing nanocatalysts in FC devices. An in-depth understanding of the electrocatalytic reaction mechanisms can guide the synthesis of optimal electrocatalysts, thereby optimizing the bonding strength between intermediate species and active sites, and enhancing the power density of fuel cells. Here, this paper outlines the latest Pt-based alloy nanomaterials, which are impor-

tant electrocatalysts for electrochemical energy conversion. These alloy nanomaterials with controlled size, shape, and composition have been widely studied as highly active and stable electrocatalysts in an attempt to reduce the required precious metal loading. Improved activity and stability of alloy catalysts can be clearly seen in the electrochemical tests and MEA systems, where the electronic effect, strain effect and ordering structure can change the activation energy barrier and reaction kinetics. Considering the obvious progress in alloy nanomaterials in terms of resistance to poisoning, stability, and activity, we are confident that more exciting work will emerge in this field.

Although alloys have made great progress in the field of electrocatalysis, there are still some challenges that seriously hinder their development. First, the electrocatalytic performance of shape-controlled nanocatalysts is often superior to that of spherical nanoparticles due to the surface sensitivity of electrochemical reactions. However, intermetallic nanocatalysts often are obtained by the annealing method, which has to minimize surface energy; the control of ordered Pt-based or Pd-based shape has been met with limited success. Therefore, rationally designing intermetallic nanocatalysts with special crystal planes may enhance the activity and selectivity of fuel cell electrocatalytic reactions. Second, the outermost surface of heterogeneous catalysts maintains the actual structure in the fuel cell electrocatalytic reactions, because the nanocatalyst surface will contact the gas and electrolyte solution (such as H_2, O_2, $HClO_4$, KOH etc.) during the reaction to cause the surface reconstruction. Third, although more desirable catalysts have been designed in the research of the rotary disk electrode (RDE), some problems occur in the actual fuel cell test systems, for example, the catalysts can hardly reach the performance of RDE, the anodic fuels pass through the membrane to the cathode, and some non-precious metal ions damage the proton exchange membrane (such as Fe-catalysed Fenton reactions), etc. Therefore, the practical application of alloy nanomaterials in fuel cells still has a long way to go.

With the development of materials engineering technologies and theoretical calculations, a large number of highly active alloy catalysts have been successfully designed. The goal of these synthetic strategies is either to improve the binding strength of reaction intermediates or to reduce the reaction energy barrier. The emergence of various high-performance alloy nanocatalysts has laid the foundation for the practical application of fuel cells, and spotlights some insights into the future directions. (1) Some electrocatalytic reaction mechanisms still lack experimental evidence and the reasons for the slow kinetic processes are still ambiguous. The solution to these problems is crucial for the design of highly active and durable nanocatalysts. Many $in\ situ$ characterization technologies (such as FTIRS, TEM, XRD, XPS, NMR, Raman, XAFS etc.) can monitor the information such as reaction species, structural changes, surface states and adsorption modes, which reveal the underlying reaction mechanism and control of active sites. (2) From the perspective of the electrochemical reaction process, the transport of reactive species through the electric double layer/water layer is very important, and few studies have proposed specific strategies in these aspects. The electronic structure of the electric double layer is closely related to the catalytic surface, so the dynamic changes of the catalyst surface in the electrolyte solution are also the main research directions in the future. (3) For the design of alloy materials, the surface structure of the catalyst must be adjusted due to surface oxidation and dissolution of non-precious metals during long-term operation. In addition to the intermetallic compounds mentioned in this article, the controlled synthesis of thin-layer carbon film-coated alloy nanoparticles, non-metal alloy nanomaterials, and high entropy alloy materials can also enhance the stability. (4) Additionally, the long-term operation of fuel cells also needs to figure out the degradation mechanism of nanomaterials, which has rarely been discussed. In general, the understanding of relevant phenomena in fundamental research, and the development of advanced alloy materials are essential for the future widespread utilization of fuel cells in daily life.

Conflicts of interest

The authors declare no conflict of interest.

Acknowledgements

References

1 J. T. L. Gamler, H. M. Ashberry, S. E. Skrabalak and K. M. Koczkur, $Adv.\ Mater.$, 2018, **30**, 1801563–18015681.
2 B.-W. Zhang, H.-L. Yang, Y.-X. Wang, S.-X. Dou and H.-K. Liu, $Adv.\ Energy\ Mater.$, 2018, **8**, 1703597–1703613.
3 H.-H. Li and S.-H. Yu, $Adv.\ Mater.$, 2019, **31**, 1803503.
4 J. K. Norskov, T. Bligaard, B. Hvolbaek, F. Abild-Pedersen, I. Chorkendorff and C. H. Christensen, $Chem.\ Soc.\ Rev.$, 2008, **37**, 2163–2171.
5 D. R. Rolison, $Science$, 2003, **299**, 1698–1701.
6 Z. W. Seh, J. Kibsgaard, C. F. Dickens, I. Chorkendorff, J. K. Norskov and T. F. Jaramillo, $Science$, 2017, **355**, 4998–5009.
7 E. Antolini, $Energy\ Environ.\ Sci.$, 2009, **2**, 915–931.
8 L. Zhang, K. Doyle-Davis and X. Sun, $Energy\ Environ.\ Sci.$, 2019, **12**, 492–517.
9 J. Jiang, W. Ding, W. Li and Z. Wei, $Chem$, 2019, **6**, 1–17.
10 M. V. Lebedeva, V. Pierron-Bohnes, C. Goyhenex, V. Papaefthimiou, S. Zafeiratos, R. R. Nazmutdinov, V. Da Costa, M. Acosta, L. Zosiak, R. Kozubski, D. Muller and E. R. Savinova, $Electrochim.\ Acta$, 2013, **108**, 605–616.

11 X.-Y. Lang, G.-F. Han, B.-B. Xiao, L. Gu, Z.-Z. Yang, Z. Wen, Y.-F. Zhu, M. Zhao, J.-C. Li and Q. Jiang, *Adv. Funct. Mater.*, 2015, **25**, 230–237.

12 W. Wang, F. Lv, B. Lei, S. Wan, M. Luo and S. Guo, *Adv. Mater.*, 2016, **28**, 10117–10141.

13 L. Wu, A. Mendoza-Garcia, Q. Li and S. Sun, *Chem. Rev.*, 2016, **116**, 10473–10512.

14 C. Zhu, D. Du, A. Eychmuller and Y. Lin, *Chem. Rev.*, 2015, **115**, 8896–8943.

15 S. Furukawa and T. Komatsu, *ACS Catal.*, 2016, **7**, 735–765.

16 M. Luo, Y. Sun, L. Wang and S. Guo, *Adv. Energy Mater.*, 2017, **7**, 1602073–1602085.

17 X. Yu, J. Zhao, L.-R. Zheng, Y. Tong, M. Zhang, G. Xu, C. Li, J. Ma and G. Shi, *ACS Energy Lett.*, 2018, **3**, 237–244.

18 Y. Yan, J. S. Du, K. D. Gilroy, D. Yang, Y. Xia and H. Zhang, *Adv. Mater.*, 2017, **29**, 1605997–1606025.

19 B. Zhang, G. Fu, Y. Li, L. Liang, N. S. Grundish, Y. Tang, J. B. Goodenough and Z. Cui, *Angew. Chem.*, 2020, **59**, 7857–7863.

20 D. Y. Chung, S. W. Jun, G. Yoon, S. G. Kwon, D. Y. Shin, P. Seo, J. M. Yoo, H. Shin, Y. H. Chung, H. Kim, B. S. Mun, K. S. Lee, N. S. Lee, S. J. Yoo, D. H. Lim, K. Kang, Y. E. Sung and T. Hyeon, *J. Am. Chem. Soc.*, 2015, **137**, 15478–15485.

21 S. Sun, C. B. Murray, D. Weller, L. Folks and A. Moser, *Science*, 2000, **287**, 1989–1992.

22 L. Bu, S. Guo, X. Zhang, X. Shen, D. Su, G. Lu, X. Zhu, J. Yao, J. Guo and X. Huang, *Nat. Commun.*, 2016, **7**, 11850–11859.

23 Z. Cui, L. Li, A. Manthiram and J. B. Goodenough, *J. Am. Chem. Soc.*, 2015, **137**, 7278–7281.

24 K. Jiang, P. Wang, S. Guo, X. Zhang, X. Shen, G. Lu, D. Su and X. Huang, *Angew. Chem., Int. Ed.*, 2016, **55**, 9030–9035.

25 C. Wang, D. P. Chen, X. Sang, R. R. Unocic and S. E. Skrabalak, *ACS Nano*, 2016, **10**, 6345–6353.

26 S. Maksimuk, S. Yang, Z. Peng and H. Yang, *J. Am. Chem. Soc.*, 2007, **129**, 8684–8685.

27 J. Shim, J. Lee, Y. Ye, J. Hwang, S.-K. Kim, T.-H. Lim, U. Wiesner and J. Lee, *ACS Nano*, 2012, **6**, 6870–6881.

28 L. Gan, C. Cui, M. Heggen, F. Dionigi, S. Rudi and P. Strasser, *Science*, 2014, **346**, 1502–1506.

29 J. Liang, F. Ma, S. Hwang, X. Wang, J. Sokolowski, Q. Li, G. Wu and D. Su, *Joule*, 2019, **3**, 956–991.

30 P. Yang, X. Yuan, H. Hu, Y. Liu, H. Zheng, D. Yang, L. Chen, M. Cao, Y. Xu, Y. Min, Y. Li and Q. Zhang, *Adv. Funct. Mater.*, 2018, **28**, 1704774–1704781.

31 J. Meier, J. Schiøtz, P. Liu, J. K. Nørskov and U. Stimming, *Chem. Phys. Lett.*, 2004, **390**, 440–444.

32 K. Elbert, J. Hu, Z. Ma, Y. Zhang, G. Chen, W. An, P. Liu, H. S. Isaacs, R. R. Adzic and J. X. Wang, *ACS Catal.*, 2015, **5**, 6764–6772.

33 Z. Qi, Y. Pei, T. W. Goh, Z. Wang, X. Li, M. Lowe, R. V. Maligal-Ganesh and W. Huang, *Nano Res.*, 2018, **11**, 3469–3479.

34 Z. Qi, C. Xiao, C. Liu, T. W. Goh, L. Zhou, R. Maligal-Ganesh, Y. Pei, X. Li, L. A. Curtiss and W. Huang, *J. Am. Chem. Soc.*, 2017, **139**, 4762–4768.

35 Y. Kang and C. B. Murray, *J. Am. Chem. Soc.*, 2010, **132**, 7568–7569.

36 Q. Chen, Y. Yang, Z. Cao, Q. Kuang, G. Du, Y. Jiang, Z. Xie and L. Zheng, *Angew. Chem., Int. Ed.*, 2016, **55**, 9021–9025.

37 K. D. Gilroy, A. Ruditskiy, H. C. Peng, D. Qin and Y. Xia, *Chem. Rev.*, 2016, **116**, 10414–10472.

38 N. S. Porter, H. Wu, Z. Quan and J. Fang, *Acc. Chem. Res.*, 2013, **46**, 1867–1877.

39 L. Vitos, A. V. Ruban, H. L. Skriver and J. Kollár, *Surf. Sci.*, 1998, **411**, 186–202.

40 S. Liu, N. Tian, A. Y. Xie, J. H. Du, J. Xiao, L. Liu, H. Y. Sun, Z. Y. Cheng, Z. Y. Zhou and S. G. Sun, *J. Am. Chem. Soc.*, 2016, **138**, 5753–5756.

41 N. Tian, Z.-Y. Zhou, S.-G. Sun, Y. Ding and Z. L. Wang, *Science*, 2007, **316**, 732–735.

42 Z. Y. Zhou, Z. Z. Huang, D. J. Chen, Q. Wang, N. Tian and S. G. Sun, *Angew. Chem., Int. Ed.*, 2010, **49**, 411–414.

43 Y. J. Mao, L. Wei, X. S. Zhao, Y. S. Wei, J. W. Li, T. Sheng, F. C. Zhu, N. Tian, Z. Y. Zhou and S. G. Sun, *Chem. Commun.*, 2019, **55**, 9335–9338.

44 W. Chen, J. Kim, S. Sun and S. Chen, *Langmuir*, 2007, **23**, 11303–11310.

45 G. V. Ramesh, R. Kodiyath, T. Tanabe, M. Manikandan, T. Fujita, N. Umezawa, S. Ueda, S. Ishihara, K. Ariga and H. Abe, *ACS Appl. Mater. Interfaces*, 2014, **6**, 16124–16130.

46 Q. Shi, C. Zhu, C. Bi, H. Xia, M. H. Engelhard, D. Du and Y. Lin, *J. Mater. Chem. A*, 2017, **5**, 23952–23959.

47 T. Bligaard and J. K. Nørskov, *Electrochim. Acta*, 2007, **52**, 5512–5516.

48 B. Hammer and J. K. Nørskov, *Surf. Sci.*, 1995, **343**, 211–220.

49 P. Liu and J. K. Nørskov, *Phys. Chem. Chem. Phys.*, 2001, **3**, 3814–3818.

50 M. Mavrikakis, B. Hammer and J. K. Nørskov, *Phys. Rev. Lett.*, 1998, **81**, 2819–2822.

51 L. Rößner and M. Armbrüster, *ACS Catal.*, 2019, **9**, 2018–2062.

52 B. T. Sneed, A. P. Young and C. K. Tsung, *Nanoscale*, 2015, **7**, 12248–12265.

53 M. Escudero-Escribano, P. Malacrida, M. H. Hansen, U. G. Vej-Hansen, A. Velázquez-Palenzuela, V. Tripkovic, J. Schiøtz, J. Rossmeisl, I. E. L. Stephens and I. Chorkendorff, *Science*, 2016, **352**, 73–76.

54 M. Escudero-Escribano, A. Verdaguer-Casadevall, P. Malacrida, U. Gronbjerg, B. P. Knudsen, A. K. Jepsen, J. Rossmeisl, I. E. Stephens and I. Chorkendorff, *J. Am. Chem. Soc.*, 2012, **134**, 16476–16479.

55 C. Wang, X. Sang, J. T. L. Gamler, D. P. Chen, R. R. Unocic and S. E. Skrabalak, *Nano Lett.*, 2017, **17**, 5526–5532.

56 L. Bu, N. Zhang, S. Guo, X. Zhang, J. Li, J. Yao, T. Wu, G. Lu, J.-Y. Ma, D. Su and X. Huang, *Science*, 2016, **354**, 1410–1414.

57 K. A. Kuttiyiel, S. Kattel, S. Cheng, J. H. Lee, L. Wu, Y. Zhu, G.-G. Park, P. Liu, K. Sasaki, J. G. Chen and R. R. Adzic, *ACS Appl. Energy Mater.*, 2018, **1**, 3771–3777.

58 J.-M. Zhang, J.-J. He, X.-Q. Wang, Y.-J. Fan, X.-J. Zhang, J.-P. Zhong, W. Chen and S.-G. Sun, *Int. J. Hydrogen Energy*, 2019, **44**, 28709–28719.

59 J.-M. Zhang, R.-X. Wang, R.-J. Nong, Y. Li, X.-J. Zhang, P.-Y. Zhang and Y.-J. Fan, *Int. J. Hydrogen Energy*, 2017, **42**, 7226–7234.

60 T. Gunji, S. H. Noh, F. Ando, T. Tanabe, B. Han, T. Ohsaka and F. Matsumoto, *J. Mater. Chem. A*, 2018, **6**, 14828–14837.

61 N. Hodnik, C. Jeyabharathi, J. C. Meier, A. Kostka, K. L. Phani, A. Recnik, M. Bele, S. Hocevar, M. Gaberscek and K. J. Mayrhofer, *Phys. Chem. Chem. Phys.*, 2014, **16**, 13610–13615.

62 J. Kim, Y. Lee and S. Sun, *J. Am. Chem. Soc.*, 2010, **132**, 4996–4997.

63 D. Strmcnik, M. Uchimura, C. Wang, R. Subbaraman, N. Danilovic, D. van der Vliet, A. P. Paulikas, V. R. Stamenkovic and N. M. Markovic, *Nat. Chem.*, 2013, **5**, 300–306.

64 J. Snyder, I. McCue, K. Livi and J. Erlebacher, *J. Am. Chem. Soc.*, 2012, **134**, 8633–8645.

65 P. Strasser, S. Koh, T. Anniyev, J. Greeley, K. More, C. Yu, Z. Liu, S. Kaya, D. Nordlund, H. Ogasawara, M. F. Toney and A. Nilsson, *Nat. Chem.*, 2010, **2**, 454–460.

66 J. Li, Z. Xi, Y. T. Pan, J. S. Spendelow, P. N. Duchesne, D. Su, Q. Li, C. Yu, Z. Yin, B. Shen, Y. S. Kim, P. Zhang and S. Sun, *J. Am. Chem. Soc.*, 2018, **140**, 2926–2932.

67 V. R. Stamenkovic, B. S. Mun, M. Arenz, K. J. Mayrhofer, C. A. Lucas, G. Wang, P. N. Ross and N. M. Markovic, *Nat. Mater.*, 2007, **6**, 241–247.

68 C. Wang, M. Chi, D. Li, D. Strmcnik, D. van der Vliet, G. Wang, V. Komanicky, K. C. Chang, A. P. Paulikas, D. Tripkovic, J. Pearson, K. L. More, N. M. Markovic and V. R. Stamenkovic, *J. Am. Chem. Soc.*, 2011, **133**, 14396–14403.

69 H. Liao, A. Fisher and Z. J. Xu, *Small*, 2015, **11**, 3221–3246.

70 B.-W. Zhang, C.-L. He, Y.-X. Jiang, M.-H. Chen, Y.-Y. Li, L. Rao and S.-G. Sun, *Electrochem. Commun.*, 2012, **25**, 105–108.

71 X. Zhang, S. Yu, L. Qiao, W. Zheng and P. Liu, *J. Chem. Phys.*, 2015, **142**, 194710.

72 B.-W. Zhang, Z.-C. Zhang, H.-G. Liao, Y. Gong, L. Gu, X.-M. Qu, L.-X. You, S. Liu, L. Huang, X.-C. Tian, R. Huang, F.-C. Zhu, T. Liu, Y.-X. Jiang, Z.-Y. Zhou and S.-G. Sun, *Nano Energy*, 2016, **19**, 198–209.

73 E. Antolini, *RSC Adv.*, 2016, **6**, 3307–3325.

74 T. Gunji, T. Tanabe, A. J. Jeevagan, S. Usui, T. Tsuda, S. Kaneko, G. Saravanan, H. Abe and F. Matsumoto, *J. Power Sources*, 2015, **273**, 990–998.

75 W. Huang, X. Kang, C. Xu, J. Zhou, J. Deng, Y. Li and S. Cheng, *Adv. Mater.*, 2018, **30**, 1706962–1706967.

76 T. Liu, K. Wang, Q. Yuan, Z. Shen, Y. Wang, Q. Zhang and X. Wang, *Nanoscale*, 2017, **9**, 2963–2968.

77 K. J. J. Mayrhofer and M. Arenz, *Nat. Chem.*, 2009, **1**, 518–519.

78 H. Liao, J. Zhu and Y. Hou, *Nanoscale*, 2014, **6**, 1049–1055.

79 J. Zheng, D. A. Cullen, R. V. Forest, J. A. Wittkopf, Z. Zhuang, W. Sheng, J. G. Chen and Y. Yan, *ACS Catal.*, 2015, **5**, 1468–1474.

80 D. Cao, G. Q. Lu, A. Wieckowski, S. A. Wasileski and M. Neurock, *J. Phys. Chem. B*, 2005, **109**, 11622–11633.

81 A. Cuesta, *J. Am. Chem. Soc.*, 2006, **128**, 13332–13333.

82 D. J. Chen and Y. J. Tong, *Angew. Chem., Int. Ed.*, 2015, **54**, 9394–9398.

83 R. Mancharan and J. B. Goodenough, *J. Mater. Chem.*, 1992, **2**, 875–887.

84 A. M. Hofstead-Duffy, D.-J. Chen, S.-G. Sun and Y. J. Tong, *J. Mater. Chem.*, 2012, **22**, 5205–5208.

85 D. Y. Chung, K.-J. Lee and Y.-E. Sung, *J. Phys. Chem. C*, 2016, **120**, 9028–9035.

86 T. Takeguchi, T. Yamanaka, K. Asakura, E. N. Muhamad, K. Uosaki and W. Ueda, *J. Am. Chem. Soc.*, 2012, **134**, 14508–14512.

87 W.-Y. Zhao, B. Ni, Q. Yuan, P.-L. He, Y. Gong, L. Gu and X. Wang, *Adv. Energy Mater.*, 2017, **7**, 1601593–1601600.

88 L. Huang, X. Zhang, Q. Wang, Y. Han, Y. Fang and S. Dong, *J. Am. Chem. Soc.*, 2018, **140**, 1142–1147.

89 J. Zhang, X. Qu, Y. Han, L. Shen, S. Yin, G. Li, Y. Jiang and S. Sun, *Appl. Catal., B*, 2019, **263**, 118345–118353.

90 U. Bardi, D. Dahlgren and P. N. Ross, *J. Catal.*, 1986, **100**, 196–209.

91 H. Abe, F. Matsumoto, L. R. Alden, S. C. Warren, H. D. Abruña and F. J. DiSalvo, *J. Am. Chem. Soc.*, 2008, **130**, 5452–5458.

92 Z. Cui, H. Chen, M. Zhao, D. Marshall, Y. Yu, H. Abruna and F. J. DiSalvo, *J. Am. Chem. Soc.*, 2014, **136**, 10206–10209.

93 J. Sanetuntikul, K. Ketpang and S. Shanmugam, *ACS Catal.*, 2015, **5**, 7321–7327.

94 E. Casado-Rivera, D. J. Volpe, L. Alden, C. Lind, C. Downie, T. Vázquez-Alvarez, A. C. D. Angelo, F. J. DiSalvo and H. D. Abruña, *J. Am. Chem. Soc.*, 2004, **126**, 4043–4049.

95 Y. Kang, J. B. Pyo, X. Ye, T. R. Gordon and C. B. Murray, *ACS Nano*, 2012, **6**, 5642–5647.

96 Q. Feng, S. Zhao, D. He, S. Tian, L. Gu, X. Wen, C. Chen, Q. Peng, D. Wang and Y. Li, *J. Am. Chem. Soc.*, 2018, **140**, 2773–2776.

97 L. Gao, X. Li, Z. Yao, H. Bai, Y. Lu, C. Ma, S. Lu, Z. Peng, J. Yang, A. Pan and H. Huang, *J. Am. Chem. Soc.*, 2019, **141**, 18083–18090.

98 S. Song and P. Tsiakaras, *Appl. Catal., B*, 2006, **63**, 187–193.

99 P. J. Rheinländer, J. Herranz, J. Durst and H. A. Gasteiger, *J. Electrochem. Soc.*, 2014, **161**, F1448–F1457.

100 T. Herranz, M. Ibáñez, J. L. Gómez de la Fuente, F. J. Pérez-Alonso, M. A. Peña, A. Cabot and S. Rojas, *ChemElectroChem*, 2014, **1**, 885–895.

101 S. Sarkar, R. Jana, S. Prasad, U. V. Waghmare, B. Thapa, S. Sampath and S. C. Peter, *Chem. Mater.*, 2015, **27**, 7459–7467.

102 H. Wang, Z. Jusys and R. J. Behm, *J. Phys. Chem. B*, 2004, **108**, 19413–19424.

103 Z. Liang, L. Song, S. Deng, Y. Zhu, E. Stavitski, R. R. Adzic, J. Chen and J. X. Wang, *J. Am. Chem. Soc.*, 2019, **141**, 9629–9636.

104 Q. Wang, G. Q. Sun, L. H. Jiang, Q. Xin, S. G. Sun, Y. X. Jiang, S. P. Chen, Z. Jusys and R. J. Behm, *Phys. Chem. Chem. Phys.*, 2007, **9**, 2686–2696.

105 R. Kavanagh, X. M. Cao, W. F. Lin, C. Hardacre and P. Hu, *Angew. Chem., Int. Ed.*, 2012, **51**, 1572–1575.

106 Z. F. Xu and Y. Wang, *J. Phys. Chem. C*, 2011, **115**, 20565–20571.

107 M. Li, P. Liu and R. R. Adzic, *J. Phys. Chem. Lett.*, 2012, **3**, 3480–3485.

108 H.-F. Wang and Z.-P. Liu, *J. Am. Chem. Soc.*, 2008, **130**, 10996–11004.

109 F. Zhu, K. Tu, L. Huang, X. Qu, J. Zhang, H. Liao, Z. Zhou, Y. Jiang and S. Sun, *Electrochim. Acta*, 2018, **292**, 208–216.

110 R. Rizo, R. M. Aran-Ais, E. Padgett, D. A. Muller, M. J. Lazaro, J. Solla-Gullon, J. M. Feliu, E. Pastor and H. D. Abruña, *J. Am. Chem. Soc.*, 2018, **140**, 3791–3797.

111 Q. Chang, S. Kattel, X. Li, Z. Liang, B. M. Tackett, S. R. Denny, P. Zhang, D. Su, J. G. Chen and Z. Chen, *ACS Catal.*, 2019, **9**, 7618–7625.

112 A. R. Miedema, R. Boom and F. R. De Boer, *J. Less-Common Met.*, 1975, **41**, 283–298.

113 R. Kodiyath, G. V. Ramesh, E. Koudelkova, T. Tanabe, M. Ito, M. Manikandan, S. Ueda, T. Fujita, N. Umezawa, H. Noguchi, K. Ariga and H. Abe, *Energy Environ. Sci.*, 2015, **8**, 1685–1689.

114 B.-W. Zhang, W.-H. Lai, T. Sheng, X.-M. Qu, Y.-X. Wang, L. Ren, L. Zhang, Y. Du, Y.-X. Jiang, S.-G. Sun and S.-X. Dou, *J. Mater. Chem. A*, 2019, **7**, 5214–5220.

115 Y. Sun, Y. Liang, M. Luo, F. Lv, Y. Qin, L. Wang, C. Xu, E. Fu and S. Guo, *Small*, 2018, **14**, 1702259–1702266.

116 J. E. Sulaiman, S. Zhu, Z. Xing, Q. Chang and M. Shao, *ACS Catal.*, 2017, **7**, 5134–5141.

117 B.-W. Zhang, T. Sheng, Y.-X. Wang, X.-M. Qu, J.-M. Zhang, Z.-C. Zhang, H.-G. Liao, F.-C. Zhu, S.-X. Dou, Y.-X. Jiang and S.-G. Sun, *ACS Catal.*, 2016, **7**, 892–895.

118 M. R. Zamanzad Ghavidel and E. B. Easton, *Appl. Catal., B*, 2015, **176–177**, 150–159.

119 D. J. Chen, Z. Y. Zhou, Q. Wang, D. M. Xiang, N. Tian and S. G. Sun, *Chem. Commun.*, 2010, **46**, 4252–4254.

120 T. Ghosh, B. M. Leonard, Q. Zhou and F. J. DiSalvo, *Chem. Mater.*, 2010, **22**, 2190–2202.

121 D. Sun, L. Si, G. Fu, C. Liu, D. Sun, Y. Chen, Y. Tang and T. Lu, *J. Power Sources*, 2015, **280**, 141–146.

122 K. Jiang, H. X. Zhang, S. Zou and W. B. Cai, *Phys. Chem. Chem. Phys.*, 2014, **16**, 20360–20376.

123 E. Casado-Rivera, Z. Gál, A. C. D. Angelo, C. Lind, F. J. DiSalvo and H. D. Abruña, *ChemPhysChem*, 2003, **4**, 193–199.

124 L. Chen, J. Zhu, C. Xuan, W. Xiao, K. Xia, W. Xia, C. Lai, H. L. Xin and D. Wang, *J. Mater. Chem. A*, 2018, **6**, 5848–5855.

125 X. Ji, K. T. Lee, R. Holden, L. Zhang, J. Zhang, G. A. Botton, M. Couillard and L. F. Nazar, *Nat. Chem.*, 2010, **2**, 286–293.

126 M. Osawa, K. Komatsu, G. Samjeske, T. Uchida, T. Ikeshoji, A. Cuesta and C. Gutierrez, *Angew. Chem., Int. Ed.*, 2011, **50**, 1159–1163.

127 Y. Kang, L. Qi, M. Li, R. E. Diaz, D. Su, R. R. Adzic, E. Stach, J. Li and C. B. Murray, *ACS Nano*, 2012, **6**, 2818–2825.

128 S. Luo, W. Chen, Y. Cheng, X. Song, Q. Wu, L. Li, X. Wu, T. Wu, M. Li, Q. Yang, K. Deng and Z. Quan, *Adv. Mater.*, 2019, **31**, 1903683–1903689.

129 J. V. Perales-Rondon, A. Ferre-Vilaplana, J. M. Feliu and E. Herrero, *J. Am. Chem. Soc.*, 2014, **136**, 13110–13113.

130 Z. Y. Zhou, J. Ren, X. Kang, Y. Song, S. G. Sun and S. Chen, *Phys. Chem. Chem. Phys.*, 2012, **14**, 1412–1417.

131 X. Qu, Z. Cao, B. Zhang, X. Tian, F. Zhu, Z. Zhang, Y. Jiang and S. Sun, *Chem. Commun.*, 2016, **52**, 4493–4496.

132 H. Rong, J. Mao, P. Xin, D. He, Y. Chen, D. Wang, Z. Niu, Y. Wu and Y. Li, *Adv. Mater.*, 2016, **28**, 2540–2546.

133 Y. T. Pan, Y. Yan, Y. T. Shao, J. M. Zuo and H. Yang, *Nano Lett.*, 2016, **16**, 6599–6603.

134 H. Xu, B. Yan, S. Li, J. Wang, C. Wang, J. Guo and Y. Du, *Chem. Eng. J.*, 2018, **334**, 2638–2646.

135 L. An, H. Yan, B. Li, J. Ma, H. Wei and D. Xia, *Nano Energy*, 2015, **15**, 24–32.

136 D. Xu, S. Bliznakov, Z. Liu, J. Fang and N. Dimitrov, *Angew. Chem., Int. Ed.*, 2010, **49**, 1282–1285.

137 Q. S. Chen, Z. Y. Zhou, F. J. Vidal-Iglesias, J. Solla-Gullon, J. M. Feliu and S. G. Sun, *J. Am. Chem. Soc.*, 2011, **133**, 12930–12933.

138 L. Huang, M. Liu, H. Lin, Y. Xu, J. Wu, V. P. Dravid, C. Wolverton and C. A. Mirkin, *Science*, 2019, **365**, 1159–1163.

139 R. Wang, J. Liu, P. Liu, X. Bi, X. Yan, W. Wang, Y. Meng, X. Ge, M. Chen and Y. Ding, *Nano Res.*, 2014, **7**, 1569–1580.

140 S. Hu, F. Munoz, J. Noborikawa, J. Haan, L. Scudiero and S. Ha, *Appl. Catal., B*, 2016, **180**, 758–765.

141 R. Jana, U. Subbarao and S. C. Peter, *J. Power Sources*, 2016, **301**, 160–169.

142 Z. Xi, J. Li, D. Su, M. Muzzio, C. Yu, Q. Li and S. Sun, *J. Am. Chem. Soc.*, 2017, **139**, 15191–15196.

143 Z. Liu, G. Fu, J. Li, Z. Liu, L. Xu, D. Sun and Y. Tang, *Nano Res.*, 2018, **11**, 4686–4696.

144 D. Liu, M. Xie, C. Wang, L. Liao, L. Qiu, J. Ma, H. Huang, R. Long, J. Jiang and Y. Xiong, *Nano Res.*, 2016, **9**, 1590–1599.

145 N. Yang, Z. Zhang, B. Chen, Y. Huang, J. Chen, Z. Lai, Y. Chen, M. Sindoro, A. L. Wang, H. Cheng, Z. Fan, X. Liu, B. Li, Y. Zong, L. Gu and H. Zhang, *Adv. Mater.*, 2017, **29**, 1700769–1700774.

146 Q. Liu, L. Du, G. Fu, Z. Cui, Y. Li, D. Dang, X. Gao, Q. Zheng and J. B. Goodenough, *Adv. Energy Mater.*, 2019, **9**, 1803040–1803046.

147 R. F. Service, *Science*, 2007, **315**, 172–172.

148 A. U. Nilekar, S. Alayoglu, B. Eichhorn and M. Mavrikakis, *J. Am. Chem. Soc.*, 2010, **132**, 7418–7428.

149 J. Durst, A. Siebel, C. Simon, F. Hasché, J. Herranz and H. A. Gasteiger, *Energy Environ. Sci.*, 2014, **7**, 2255–2260.

150 I. E. L. Stephens, J. Rossmeisl and I. Chorkendorff, *Science*, 2016, **354**, 1378–1379.

151 X. Li and K. Lu, *Science*, 2019, **364**, 733–734.

152 B.-A. Lu, T. Sheng, N. Tian, Z.-C. Zhang, C. Xiao, Z.-M. Cao, H.-B. Ma, Z.-Y. Zhou and S.-G. Sun, *Nano Energy*, 2017, **33**, 65–71.

153 Z. Wang, X. Yao, Y. Kang, L. Miao, D. Xia and L. Gan, *Adv. Funct. Mater.*, 2019, **29**, 1902987–1902995.

154 Y. Bing, H. Liu, L. Zhang, D. Ghosh and J. Zhang, *Chem. Soc. Rev.*, 2010, **39**, 2184–2202.

155 V. Čolić and A. S. Bandarenka, *ACS Catal.*, 2016, **6**, 5378–5385.

156 X. X. Du, Y. He, X. X. Wang and J. N. Wang, *Energy Environ. Sci.*, 2016, **9**, 2623–2632.

157 L. Zou, J. Li, T. Yuan, Y. Zhou, X. Li and H. Yang, *Nanoscale*, 2014, **6**, 10686–10692.

158 M. K. Debe, *Nature*, 2012, **486**, 43–51.

159 T. Cheng, X.-Y. Lang, G.-F. Han, R.-Q. Yao, Z. Wen and Q. Jiang, *J. Mater. Chem. A*, 2016, **4**, 18878–18884.

160 J. Greeley, I. E. Stephens, A. S. Bondarenko, T. P. Johansson, H. A. Hansen, T. F. Jaramillo, J. Rossmeisl, I. Chorkendorff and J. K. Norskov, *Nat. Chem.*, 2009, **1**, 552–556.

161 D. Zhang, F. Wu, M. Peng, X. Wang, D. Xia and G. Guo, *J. Am. Chem. Soc.*, 2015, **137**, 6263–6269.

162 E. Antolini, *Appl. Catal., B*, 2017, **217**, 201–213.

163 S. Prabhudev, M. Bugnet, C. Bock and G. A. Botton, *ACS Nano*, 2013, **7**, 6103–6110.

164 Y. Qin, M. Luo, Y. Sun, C. Li, B. Huang, Y. Yang, Y. Li, L. Wang and S. Guo, *ACS Catal.*, 2018, **8**, 5581–5590.

165 W. Xia, A. Mahmood, Z. Liang, R. Zou and S. Guo, *Angew. Chem., Int. Ed.*, 2016, **55**, 2650–2676.

166 Z. Zhao, C. Chen, Z. Liu, J. Huang, M. Wu, H. Liu, Y. Li and Y. Huang, *Adv. Mater.*, 2019, **31**, 1808115–1808130.

167 L. Ou and S. Chen, *J. Phys. Chem. C*, 2013, **117**, 1342–1349.

168 G. Wang, Z. Yang, Y. Du and Y. Yang, *Angew. Chem., Int. Ed.*, 2019, **58**, 15848–15854.

169 J.-C. Dong, X.-G. Zhang, V. Briega-Martos, X. Jin, J. Yang, S. Chen, Z.-L. Yang, D.-Y. Wu, J. M. Feliu, C. T. Williams, Z.-Q. Tian and J.-F. Li, *Nat. Energy*, 2018, **4**, 60–67.

170 X. Tian, X. Zhao, Y.-Q. Su, L. Wang, H. Wang, D. Dang, B. Chi, H. Liu, E. J. M. Hensen, X. W. Lou and B. Y. Xia, *Science*, 2019, **366**, 850–856.

171 J. Li, S. Sharma, X. Liu, Y.-T. Pan, J. S. Spendelow, M. Chi, Y. Jia, P. Zhang, D. A. Cullen, Z. Xi, H. Lin, Z. Yin, B. Shen, M. Muzzio, C. Yu, Y. S. Kim, A. A. Peterson, K. L. More, H. Zhu and S. Sun, *Joule*, 2019, **3**, 124–135.

172 X. X. Wang, S. Hwang, Y. T. Pan, K. Chen, Y. He, S. Karakalos, H. Zhang, J. S. Spendelow, D. Su and G. Wu, *Nano Lett.*, 2018, **18**, 4163–4171.

173 Y. Feng, Q. Shao, F. Lv, L. Bu, J. Guo, S. Guo and X. Huang, *Adv. Sci.*, 2020, **7**, 1800178–1800185.

174 D. Sun, Y. Wang, K. J. T. Livi, C. Wang, R. Luo, Z. Zhang, H. Alghamdi, C. Li, F. An, B. Gaskey, T. Mueller and A. S. Hall, *ACS Nano*, 2019, **13**, 10818–10825.

175 D. Wang, H. L. Xin, H. Wang, Y. Yu, E. Rus, D. A. Muller, F. J. DiSalvo and H. D. Abruña, *Chem. Mater.*, 2012, **24**, 2274–2281.

176 Z. Cui, H. Chen, M. Zhao and F. J. DiSalvo, *Nano Lett.*, 2016, **16**, 2560–2566.

177 G. Jiang, H. Zhu, X. Zhang, B. Shen, L. Wu, S. Zhang, G. Lu, Z. Wu and S. Sun, *ACS Nano*, 2015, **9**, 11014–11022.

178 K. A. Kuttiyiel, K. Sasaki, D. Su, L. Wu, Y. Zhu and R. R. Adzic, *Nat. Commun.*, 2014, **5**, 5185–5192.

179 M. Luo, Z. Zhao, Y. Zhang, Y. Sun, Y. Xing, F. Lv, Y. Yang, X. Zhang, S. Hwang, Y. Qin, J. Y. Ma, F. Lin, D. Su, G. Lu and S. Guo, *Nature*, 2019, **574**, 81–85.

180 R. Chattot, O. Le Bacq, V. Beermann, S. Kuhl, J. Herranz, S. Henning, L. Kuhn, T. Asset, L. Guetaz, G. Renou, J. Drnec, P. Bordet, A. Pasturel, A. Eychmuller, T. J. Schmidt, P. Strasser, L. Dubau and F. Maillard, *Nat. Mater.*, 2018, **17**, 827–833.

181 P. Strasser and S. Kühl, *Nano Energy*, 2016, **29**, 166–177.

182 D. Wang, H. L. Xin, Y. Yu, H. Wang, E. Rus, D. A. Muller and H. D. Abruña, *J. Am. Chem. Soc.*, 2010, **132**, 17664–17666.

183 W. Xiao, M. A. L. Cordeiro, G. Gao, A. Zheng, J. Wang, W. Lei, M. Gong, R. Lin, E. Stavitski, H. L. Xin and D. Wang, *Nano Energy*, 2018, **50**, 70–78.

184 Y. Xiong, Y. Yang, F. J. DiSalvo and H. D. Abruna, *J. Am. Chem. Soc.*, 2018, **140**, 7248–7255.

185 G. Wang, B. Huang, L. Xiao, Z. Ren, H. Chen, D. Wang, H. D. Abruna, J. Lu and L. Zhuang, *J. Am. Chem. Soc.*, 2014, **136**, 9643–9649.

186 S. Liu, W. Xiao, J. Wang, J. Zhu, Z. Wu, H. Xin and D. Wang, *Nano Energy*, 2016, **27**, 475–481.

187 Y. Yang, W. Xiao, X. Feng, Y. Xiong, M. Gong, T. Shen, Y. Lu, H. D. Abruna and D. Wang, *ACS Nano*, 2019, **13**, 5968–5974.

188 J. Durst, A. Siebel, C. Simon, F. Hasché, J. Herranz and H. A. Gasteiger, *Energy Environ. Sci.*, 2014, **7**, 2255–2260.

189 W. Sheng, H. A. Gasteiger and Y. Shao-Horn, *J. Electrochem. Soc.*, 2010, **157**, B1529–B1536.

190 S. J. Lee, S. Mukerjee, E. A. Ticianelli and J. McBreen, *Electrochim. Acta*, 1999, **44**, 3283–3293.

191 Z.-C. Zhang, X.-C. Tian, B.-W. Zhang, L. Huang, F.-C. Zhu, X.-M. Qu, L. Liu, S. Liu, Y.-X. Jiang and S.-G. Sun, *Nano Energy*, 2017, **34**, 224–232.

192 S. St John, R. W. Atkinson, R. R. Unocic, T. A. Zawodzinski and A. B. Papandrew, *J. Phys. Chem. C*, 2015, **119**, 13481–13487.

193 T. Takeguchi, T. Yamanaka, K. Asakura, E. N. Muhamad, K. Uosaki and W. Ueda, *J. Am. Chem. Soc.*, 2012, **134**, 14508–14512.

194 Y. C. Hsieh, Y. Zhang, D. Su, V. Volkov, R. Si, L. Wu, Y. Zhu, W. An, P. Liu, P. He, S. Ye, R. R. Adzic and J. X. Wang, *Nat. Commun.*, 2013, **4**, 2466.

195 G. Shi, H. Yano, D. A. Tryk, M. Matsumoto, H. Tanida, M. Arao, H. Imai, J. Inukai, A. Iiyama and H. Uchida, *Catal. Sci. Technol.*, 2017, **7**, 6124–6131.

196 G. Shi, H. Yano, D. A. Tryk, A. Iiyama and H. Uchida, *ACS Catal.*, 2017, **7**, 267–274.

197 H. Igarashi, T. Fujino, Y. Zhu, H. Uchida and M. Watanabe, *Phys. Chem. Chem. Phys.*, 2001, **3**, 306–314.

198 T. Wang, Z.-X. Chen, S. Yu, T. Sheng, H.-B. Ma, L.-N. Chen, M. Rauf, H.-P. Xia, Z.-Y. Zhou and S.-G. Sun, *Energy Environ. Sci.*, 2018, **11**, 166–171.

199 W. Sheng, M. Myint, J. G. Chen and Y. Yan, *Energy Environ. Sci.*, 2013, **6**, 1509.

200 X. Wang, Y. Zhu, A. Vasileff, Y. Jiao, S. Chen, L. Song, B. Zheng, Y. Zheng and S.-Z. Qiao, *ACS Energy Lett.*, 2018, **3**, 1198–1204.

201 J. Chen, J. Wang, J. Chen and L. Wang, *J. Mater. Sci.*, 2017, **52**, 13064–13077.

202 P. Wang, X. Zhang, J. Zhang, S. Wan, S. Guo, G. Lu, J. Yao and X. Huang, *Nat. Commun.*, 2017, **8**, 14580.

203 I. Ledezma-Yanez, W. D. Z. Wallace, P. Sebastián-Pascual, V. Climent, J. M. Feliu and M. T. M. Koper, *Nat. Energy*, 2017, **2**, 17031.

204 Y. Cong, B. Yi and Y. Song, *Nano Energy*, 2018, **44**, 288–303.

205 J. N. Schwämmlein, B. M. Stühmeier, K. Wagenbauer, H. Dietz, V. Tileli, H. A. Gasteiger and H. A. El-Sayed, *J. Electrochem. Soc.*, 2018, **165**, H229–H239.

206 A. J. Medford, A. Vojvodic, J. S. Hummelshøj, J. Voss, F. Abild-Pedersen, F. Studt, T. Bligaard, A. Nilsson and J. K. Nørskov, *J. Catal.*, 2015, **328**, 36–42.

207 W. Sheng, Z. Zhuang, M. Gao, J. Zheng, J. G. Chen and Y. Yan, *Nat. Commun.*, 2015, **6**, 5848.

208 H. Wang and H. D. Abruna, *J. Am. Chem. Soc.*, 2017, **139**, 6807–6810.

209 Y. Wang, G. Wang, G. Li, B. Huang, J. Pan, Q. Liu, J. Han, L. Xiao, J. Lu and L. Zhuang, *Energy Environ. Sci.*, 2015, **8**, 177–181.

210 S. Lu and Z. Zhuang, *J. Am. Chem. Soc.*, 2017, **139**, 5156–5163.

211 D. Strmcnik, M. Uchimura, C. Wang, R. Subbaraman, N. Danilovic, D. van der Vliet, A. P. Paulikas, V. R. Stamenkovic and N. M. Markovic, *Nat. Chem.*, 2013, **5**, 300–306.

212 J. Li, S. Ghoshal, M. K. Bates, T. E. Miller, V. Davies, E. Stavitski, K. Attenkofer, S. Mukerjee, Z.-F. Ma and Q. Jia, *Angew. Chem., Int. Ed.*, 2017, **56**, 15594–15598.

213 L.-F. Shen, B.-A. Lu, X.-M. Qu, J.-Y. Ye, J.-M. Zhang, S.-H. Yin, Q.-H. Wu, R.-X. Wang, S.-Y. Shen, T. Sheng, Y.-X. Jiang and S.-G. Sun, *Nano Energy*, 2019, **62**, 601–609.